DRAFT VERSION SEPTEMBER 4, 2014
Preprint typeset using LaTeX style emulateapj v. 5/2/11

arXiv:1409.0916v1 [astro-ph.GA] 2 Sep 2014

IONIZATION MODELING ASTROPHYSICAL GASEOUS STRUCTURES. I. THE OPTICALLY THIN REGIME

CHRISTOPHER W. CHURCHILL[1], ELIZABETH KLIMEK[1], AMBER MEDINA[1], AND JACOB R. VANDER VLIET[1],

Draft version September 4, 2014

ABSTRACT

We present a code for modeling the ionization conditions of optically thin astrophysical gas structures. Given the gas hydrogen density, equilibrium temperature, elemental abundances, and the ionizing spectrum, the code solves the equilibrium ionization fractions and number densities for all ions from hydrogen to zinc. The included processes are photoionization, Auger ionization, direct collisional ionization, excitation auto-ionization, charge exchange ionization, two-body radiative recombination, dielectronic recombination, and charge exchange recombination. The ionizing spectrum can be generalized to include the ultraviolet background (UVB) and/or Starburst99 stellar populations of various masses, ages, metallicities, and distances. The ultimate goal with the code is to provide fast computation of the ionization conditions of gas in N-body + hydrodynamics cosmological simulations, in particular adaptive mesh refinement codes, in order to facilitate absorption line analysis of the simulated gas for comparison with observations. To this end, we developed a method to linearize the rate equations and efficiently solve the rate matrix with a minimum number of iterations. Comparing the code to Cloudy 13.03 (Ferland), we find that the hydrogen and helium ionization fractions and the metal species ionization corrections are in excellent agreement. We discuss the science drivers and plans for further development of the ionization code to a full radiative hydrodynamic routine that can be employed for processing the simulations. A stand-alone version of the code has been made publicly available.

Subject headings: galaxies: formation, evolution, halos; (galaxies:) quasars: absorption lines; radiative transfer

1. INTRODUCTION

The evolution of galaxies is intimately linked to their gas processes. Star formation rates are sustained by accretion of infalling gas (e.g., Sánchez Almeida et al. 2014) and regulated by stellar feedback processes (e.g., Stinson et al. 2007; Ceverino & Klypin 2009; Ceverino et al. 2013; Hopkins et al. 2013a,b; Kim et al. 2013; Trujillo-Gomez et al. 2013). Accretion and feedback likely persist in a stochastic quasi-balancing act that regulates galaxy evolution and yields the global properties of galaxies (e.g., Davé et al. 2011a,b; Lilly et al. 2013), such as the stellar mass-halo mass relation and the average star formation history, both a function of halo mass and redshift (e.g., Behroozi et al. 2010, 2013; Moster et al. 2013), the stellar mass-metallicity relation (e.g., Tremonti et al. 2004; Mannucci et al. 2010; Bothwell et al. 2013; González Delgado et al. 2014), and the distribution of galaxies on the color-stellar mass diagram (e.g., Schawinski et al. 2014).

With deeper appreciation for the key role gas plays in governing the evolution of galaxies, concentrated effort has been focused on incorporating increasingly sophisticated treatment of hydrodynamics and stellar formation and feedback processes in cosmological simulations. The ultimate goal is to form realistic galaxies having properties consistent with global galaxy relations while gaining insight into the physics that yields these relations (e.g., Ceverino & Klypin 2009; Ceverino et al. 2013; Hopkins et al. 2013a; Munshi et al. 2013; Trujillo-Gomez et al. 2013; Agertz & Kravtsov 2014).

Since the flow of gas in and around galaxies is central to regulating the evolution of galaxies, it is imperative the properties of this "circumgalactic medium" (CGM) associated with simulated galaxies also match observations (e.g., Ford et al. 2013a,b; Hummels et al. 2013; Churchill et al. 2014).

The CGM is observed using absorption lines in the spectra of luminous background sources, such as quasars, whose lines of sight serendipitously probe the vicinity of foreground galaxies. Commonly observed absorption lines include HI Lyα λ1215 (e.g., Lanzetta et al. 1995; Stocke et al. 2013; Tumlinson et al. 2013; Mathes et al. 2014), the CIV $\lambda\lambda$1548, 1550 and OVI $\lambda\lambda$1031, 1037 doublets (e.g., Simcoe et al. 2006; Stocke et al. 2006; Fox et al. 2007a,b; Tumlinson et al. 2011; Stocke et al. 2013; Mathes et al. 2014), and the MgII $\lambda\lambda$2796, 2803 doublet (e.g., Nielsen et al. 2013a,b, and references therein). Commonly measured absorption line quantities include the equivalent widths, column densities, the velocity spreads, the line-of-sight velocities with respect to the presumed host galaxy, and, if Voigt profile (VP) decomposition is undertaken, the number of VP components and their column densities, velocities, and Doppler *b* parameters (line profile broadening and indicator of gas temperature and turbulence). On a sightline by sightline basis, these quantities can be examined as a function of host galaxy properties (masses, luminosities, colors, star formation rates, etc.) and projected distance from the host galaxies.

Since the absorption occurs from ionized atoms and is proportional to the product of the ion density and line of sight pathlength through the gas, ionization modeling is required to infer the hydrogen density and metallicity of the CGM absorbing gas from observed spectra. The most commonly employed ionization code is Cloudy (Ferland et al. 1998, 2013). Assuming the spectral energy distribution (SED) of the ionizing spectrum is known, and assuming a cloud geometry, Cloudy allows the ionization conditions, metallicity, and hydrogen density to be constrained from the measured column densities. Usually, a Haardt & Madau (2011) ultraviolet background (UVB) ionizing spectrum is assumed for the model clouds.

Ionization modeling is equally critical for the simulations.

[1] New Mexico State University, MSC 4500, Las Cruces, NM 88003, USA

Since analysis of the simulated CGM requires a comparison with observed absorption line properties, we are required to generate synthetic absorption profiles of "sightlines" through the simulated CGM. This requires that the ionization fractions of the absorbing ions are known. There are two approaches. The first is post-process ionization modeling of the simulation output. The second is incorporation of the ionization modeling self-consistently into the hydrodynamics of the cosmological simulation, which is computationally expensive.

For both observations and simulations, several assumptions are often employed, most importantly that the gas is in ionization equilibrium and that the SED of the ionizing spectrum is known, at least approximately. In the CGM, the ionizing SED can have substantial variations, both temporally and spatially. Since the ionization conditions strongly depend on the density and temperature of the simulated gas, it is important the heating and cooling rates are as realistic as possible. However, the heating and cooling rates depend upon the ionizing SED, the gas density, temperature, and the atomic abundances of metals in the gas. If the cooling time is shorter than the ionization and/or recombination timescales of a given ion, then that ion cannot settle into ionization equilibrium. These considerations highlight the importance for incorporating a spatially resolved radiative transfer (RT) scheme that is coupled to the hydrodynamics in cosmological simulations (hereafter, radiation hydrodynamics, RH, see Mihalas & Mihalas 1999).

Various explorations, often focused on specific astrophysical problems, have been researched to examine the effects of implementing RT and RH in hydrodynamic simulations (Howell & Greenough 2003; Iliev et al. 2006, 2009; Whalen & Norman 2006; Aubert & Teyssier 2008; Finlator et al. 2009; Norman et al. 2009; Reynolds et al. 2009). In fact, progress has been made toward incorporating RH into some cosmological simulations, either by solving the optically thin variable Eddington tensor (Gnedin & Abel 2001; Razoumov et al. 2006; Petkova & Springel 2009; Rosdahl et al. 2013), or by employing ray-tracing methods (Abel & Wandelt 2002; Wise & Abel 2011). Typically, only hydrogen and helium ionization balance is treated. However, Cen & Fang (2006) studied the evolution of O IV to O IX by directly integrating the rate equations using RH in their simulations. Oppenheimer & Schaye (2013) implemented RH into their simulations and incorporated a rate matrix including several important metals species, but so far they have limited their analysis to a single parcel of gas independent of hydrodynamics.

To date, studies of the simulated CGM that employ the absorption line technique have implemented the post-processing approach (e.g., Ford et al. 2013a,b; Hummels et al. 2013; Churchill et al. 2014). Typically, the ionization code Cloudy is used to create a grid of "cloud" models as a function of redshift assuming the Haardt & Madau (2011) UVB ionizing SED for a range of gas-state variables. The cloud models usually are constant density with a plane parallel geometry, are illuminated by the ionizing SED on one face, and omit dust and cosmic ray heating. The ionization condition of the cloud model is normally specified by the ionization parameter,

$$U = \frac{n_\gamma}{n_{\rm H}} = \frac{4\pi}{n_{\rm H}} \int_{\nu_0}^{\infty} \frac{J_\nu}{h\nu}\, d\nu\,, \qquad (1)$$

which is defined at the illuminated edge of the cloud model, where $n_{\rm H}$ is the constant hydrogen density, J_ν is specific intensity of the ionizing SED, and $h\nu_0$ is the ionization threshold energy for neutral hydrogen. Since Cloudy solves the RT through a multi-zone cloud model, the ionization structure can vary with depth into the cloud. The standard output of Cloudy are the zone-depth weighted *average* ionization fractions. A fixed metallicity and abundance pattern (usually solar) is adopted. For a given parcel of gas in the simulations, the Cloudy grid serves as a look-up table for ionization fractions, from which the metallicity and abundance pattern can be scaled (e.g., Bergeron & Stasińska 1986; Dittmann & Koeppen 1995) to yield the column density of desired ions required for generating synthetic absorption line spectra.

Ford et al. (2013a) employ a post-processing scheme in which they use Cloudy 08.00 look-up tables to determine the metal species ionization fractions as a function of density, temperature, and the UVB ionizing spectrum. For gas particles with large neutral hydrogen column densities, i.e., $N(\mathrm{H\,I}) > 18$, they incorporate a correction factor for self-shielding by matching the neutral hydrogen fractions to the models of Faucher-Giguère et al. (2009). They assume all of the column density from the Mg^+ ion arises in the self-shielded region. Hummels et al. (2013) track the hydrogen and helium ionization states within their simulations, and then use a Cloudy 07.02.01 look-up table to determine the post-processed ionization fraction of the metal ions as a function of density, temperature, and UVB ionizing spectrum. Whereas Ford et al. (2013a,b) post-processed only their line of sight quantities, Hummels et al. (2013) post-processed their full simulation output and obtain the spatial distribution of the ionic species.

Using a somewhat different approach, Fumagalli et al. (2011) adopted a post-processing Monte-Carlo RT method that removes the "preferred" direction of the photon path inherent in Cloudy by accounting for scattering. Like Cloudy, their code includes collisional ionization and photoionization, however they explore photoionization from both the UVB and local stellar sources. They focus on neutral hydrogen column densities and absorption profiles, though they did make rough estimates of Si II column densities and absorption strengths. They post-processed their full simulation output and explored the effects of the various ionization mechanisms on the spatial distribution of $N(\mathrm{H\,I})$ in the vicinity of simulated galaxies by examining the differences between collisional ionization only models, collisional plus UVB photoionization models, and models that incorporate collisional and UVB plus stellar photoionization.

Churchill et al. (2014) applied an ionization code of their own design to post-process the ionization conditions of their full simulation output and conducted a pilot study of how well the inferred conditions of the gas from simulated absorption lines compared with the actual properties of the gas giving rise to the absorption. Our goal with this paper, is to present the details of the ionization code employed by Churchill et al. (2014). The code, called the hydroART Radiative Algorithm for Trace Elements (HARTRATE), is designed to ultimately be adaptable and implemented as post-processing RH for cosmological simulations, especially the Eulerian N-body hydrodynamic code hydroART (Kravtsov 1999; Kravtsov et al. 2004). Currently, HARTRATE is applied as a post-processing step to the full simulation output but does not yet include RT nor RH through the simulation box.

In Section 2, we describe the fundamental characteristics of the hydroART code and our current approach to post-process ionization modeling. In Section 3, we detail the physics incor-

porated into the HARTRATE and the method of solution for the rate matrix. We compare isolated HARTRATE cloud models to those from the "industry standard" code Cloudy 13.03 in Section 5. In Section 6, we provide a general summary, including a description of planned future growth and implementation of HARTRATE. In addition to the first results from an application of HARTRATE to the hydroART simulations presented in Churchill et al. (2014), a stand alone version of the code has been successfully applied to observed absorption line systems by Kacprzak et al. (2012) and Churchill et al. (2012).

2. HYDRODYNAMIC SIMULATIONS

Underlying all hydrodynamic cosmological simulations is the gravitating dark matter in an expanding simulation box, which is reduced to an N-body problem that is commonly solved using hierarchical multipole expansion (tree algorithms). The baryons are usually treated as an ideal fluid so that one can simplify the hydrodynamics in terms of the Euler and continuity equations as governed by the first law of thermodynamics. Two main numerical methods are employed to solve the coupled system of collisional baryonic matter and collisionless dark matter: the particle methods, which discretize mass, and grid-based methods, which discretize space.

A popular particle based method is smoothed particle hydrodynamics, or SPH, which solves the Lagrangian form of the Euler equations. Because the gas is discretized into particles, SPH can achieve good spatial resolutions in high-density regions, but is not as robust in low-density regions. It also suffers from resolution degradation in shock regions due to artificial viscosity (Agerts et al. 2007).

Alternatively, Eulerian grid-based methods solve the hydrodynamic equations across a structured grid; each grid cell contains constant properties (density, temperature, velocity, etc.) and represents a finite volume of the gas fluid. Grid-based methods are effective in both high- and low-density regions and can handle shocks (Dolag et al. 2008). In the cosmological setting, adaptive mesh refinement (AMR), in which grid cells vary in size in inverse proportion to the gas density, are employed to increase the resolution in regions of rapid evolution while optimizing the number of cells and computational demands.

For our studies of the simulated CGM, we use the Eulerian N-body hydrodynamic code hydroART (Kravtsov 1999; Kravtsov et al. 2004). The hydroART code follows the evolution of a gravitating N-body dark matter halo and models the baryons using Eulerian hydrodynamics; it is a grid-based AMR code that uses the zoom-in technique of Klypin et al. (2001) and includes all of the currently relevant physics of galaxy formation (Ceverino & Klypin 2009; Ceverino et al. 2010, 2012, 2013; Trujillo-Gomez et al. 2013).

Stars are formed deterministically with the observed low efficiency in the cold and dense gas of molecular cloud environments. A stellar particle represents a population of stars with a given mass, age, and metallicity. As the particles age, their mass decreases as supernovae are converted back into gas. The stellar feedback model includes the major contributions from photoionization heating, direct radiation pressure, energy from type II and type Ia supernovae, and stellar winds (see Trujillo-Gomez et al. 2013, for the most recent star formation and feedback recipes).

The high-resolution region around the galaxy is typically $\sim$ 1–2 Mpc across. The hydrodynamics is resolved with $\simeq 7 \times 10^6$ grid cells, with a minimum cell size of roughly 30 h^{-1} pc at $z = 0$. At each grid cell, the hydroART code follows the evolution of the density, temperature, velocity, and metal mass fraction. The metals produced in type II and Ia supernovae are followed separately and are self-consistently advected with the gas flow.

The heating and cooling balance of the gas is determined using heating and cooling functions obtained from Cloudy 8.00 (see Ceverino et al. 2013). These account for stellar ionizing SEDs (as appropriate to the location and density of the grid cell and the ages, masses, and metallicities of the stellar particles), ionization by the UVB, molecular line cooling, and self-shielding of high column density gas. The treatment is similar to that implemented by Wiersma et al. (2009), but also includes the effects of ionization by stellar radiation.

2.1. *Treatment of Ionization Balance*

We developed a code (HARTRATE) that performs equilibrium ionization calculations in hydroART grid cells, with the goal of incorporating it as a full RH treatment. The main motivation for the development of HARTRATE is to apply it to AMR cosmological simulation in order to study the chemical and ionization conditions of the circumgalactic medium in simulated galaxies using absorption line techniques (see Churchill et al. 2014). The code we present here computes the equilibrium ionization fractions and number densities of the ions in the gas, and is currently applied as a post-processing step.

We treat each grid cell as an isolated "cloudlette". The three important gas properties associated with a cell are (1) the hydrogen density, $n_{\rm H}$, (2) the equilibrium temperature, T, and (3) the abundances of all atomic species. In order to treat photoionization processes, the spectral energy distribution (SED) of the ionizing radiation must also be specified, which requires (4) the redshift, z, which provides the cosmic epoch of the UVB ionizing radiation. In addition, the option to include stellar radiation is provided, which requires (5) the characteristics (mass, age, metallicity, and locations) of stellar populations. When applied to hydroART, the stellar populations are drawn from the stellar particles in the simulated galaxy.

The present version of HARTRATE does not treat RT through the grid cell, so there is no ionization structure within the grid cells (see Section 4). As such, currently, there is no assumption about the gas geometry. However, note that the commonly employed ionization parameter (Eq. 1) is well defined and can be easily computed from the above inputs.

3. THE IONIZATION MODEL

The ionization code HARTRATE calculates the equilibrium electron density and the ionization fractions of all ions, from which all ionic number densities are computed in each grid cell. Metals up to and including zinc are incorporated, however, the user can select which metals are included in the chemical mixture. All ions are treated as two-level systems, a bound ground state and the continuum; no recombination transitions are incorporated. Neither photo-heating nor cooling is treated, since these are directly incorporated into hydroART and yield the equilibrium temperature of the gas in the grid cells. Fumagalli et al. (2011) examined the effects of additional heating by artificially incrementing the temperatures of the grid cells and found that the morphology of the neutral hydrogen gas was negligibly modified for photoionized gas.

The equilibrium solution requires solving a matrix of coupled non-linear rate equations. We derived a method in which

the rate equations are linearized and the solution is obtained via iterative convergence on the equilibrium ionization fractions using particle and charge density conservation.

The physical gas processes included in HARTRATE are photoionization, Auger ionization, direct collisional ionization, excitation auto-ionization, charge exchange ionization, radiative recombination, dielectronic recombination, and charge exchange recombination. If desired, the effects of each of these processes can be isolated by turning the process "off" or "on".

3.1. *Notation and Formalism*

For what follows, we denote the atomic species by the index k, where k equals the atomic number, and denote the ionization stage by the index j, where $j = 1$ is the neutral stage and $j = k+1$ is the fully ionized stage. We assume that all ions and neutral atoms are in their ground state. The number density [cm^{-3}] of ion k, j is $n_{\rm k,j}$ and the electron number density is $n_{\rm e}$.

The rate equation, $dn_{\rm k,j}/dt$, quantifies the rate of change in the number of ion k, j per unit volume per unit time [cm^{-3} s^{-1}]. It can be expressed as

$$\frac{dn_{\rm k,j}}{dt} = (\text{creation rate ion } k,j) - (\text{destruction rate of ion } k,j)\,. \quad (2)$$

Clearly, there is a rate equation for each ionization stage for each atomic species, which taken together form a rate matrix. The rate matrix is closed by particle and charge density conservation.

The creation and destruction rates per unit volume are determined by multiplying the rate per unit time [s^{-1}] by the number density of the initial state particle. For example, in the case of photoionization (denoted "ph") of ion $k.j$, the contribution to the destruction rate per unit volume is $n_{\rm k,j}R^{\rm ph}_{\rm k,j}$. In the case of recombination (denoted "rec") with ion $k, j-1$ to create ion k, j, the contribution to the creation rate per unit volume is $n_{\rm k,j\text{-}1}R^{\rm rec}_{\rm k,j\text{-}1}$. Note that all rates, $R_{\rm k,j}$, are indexed to the initial ion stage.

All collision based rates are determined from the rate coefficients [cm^3 s^{-1}]. We denote ionization rate coefficients as $\alpha_{\rm k,j}$ and recombination rate coefficients as $\beta_{\rm k,j}$. In the case that ionization is due to a collision with a free electron, the rate per unit time is obtained by multiplying the rate coefficient by the electron density. We use the convention that ionization rate coefficients are indexed by referencing the initial ion stage j, whereas, for recombination, j refers to the final ion stage. That is, for recombination, rate coefficients index the ion towards which recombination proceeds.

For example, in the case of direct collisional ionization (denoted "cdi") of ion k, j by a free electron, the contribution to the destruction rate per unit volume of ion k, j is $n_{\rm k,j}R^{\rm cdi}_{\rm k,j} = n_{\rm k,j}n_{\rm e}\alpha^{\rm cdi}_{\rm k,j}$. In the case of radiative recombination (denoted "phr") of a free electron with ion k, j to create ion $k, j-1$, the contribution to the destruction rate per unit volume of ion k, j is $n_{\rm k,j}R^{\rm phr}_{\rm k,j} = n_{\rm k,j}n_{\rm e}\beta^{\rm phr}_{\rm k,j\text{-}1}$. Note that this expression would also be the contribution to the radiative recombination creation rate per unit volume for ion $k, j-1$

In Section 3.7, we write out the rate equations for all ions. The equilibrium balance is achieved when $dn_{\rm k,j}/dt = 0$ for all ions, by balancing the creation and destruction rates per unit volume. In Section 3.8, we outline our method to solve the rate matrix.

3.2. *Particle and Charge Density Conservation*

Together, particle and charge density conservation provide the constraints for obtaining the ion densities and ionization fractions.

The total number density of all ions and free electrons is $n_{\rm tot} = n_{\rm A} + n_{\rm e}$, where $n_{\rm e}$ is the density of free electrons and, as dictated by particle conservation,

$$n_{\rm A} = \sum_{\rm k=1} n_{\rm k} = \sum_{\rm k=1} \sum_{\rm j=1}^{\rm k+1} n_{\rm k,j}\,, \quad (3)$$

is the number density of all atomic species, where $n_{\rm k}$ is the number densities of species k, and $n_{\rm k,j}$ is the number density of species k in ionization stage j. Since the ionization model includes elements only up to zinc, the maximum k is 30. And, since the user can specify a subset of these elements for inclusion into the ionization model, the sum includes only the k values of the atomic species used in the ionization model.

The abundance fractions, $\eta_{\rm k} = n_{\rm k}/n_{\rm A}$, are employed to compute the number density of the atomic species. With this formalism, the number density of each atomic species is determined directly from the input hydrogen number density and abundance fractions via $n_{\rm k} = \eta_{\rm k}n_{\rm A} = (\eta_{\rm k}/\eta_{\rm H})n_{\rm H}$, where $\eta_{\rm H} \equiv \eta_1$ and $n_{\rm H} \equiv n_1$. The $\eta_{\rm k}$ are determined by the mass fractions, $x_{\rm k}$, according to

$$\eta_{\rm k} = \frac{x_{\rm k}/A_{\rm k}}{\sum_{\rm k=1} x_{\rm k}/A_{\rm k}}\,, \quad (4)$$

where $A_{\rm k}$ is the atomic mass of species k in units of the unified atomic mass unit, $m_{\rm a} = 1.6605 \times 10^{-24}$ [g]. Again, the sum includes only the elements used in the ionization model in order to preserve $\sum_{\rm k=1} \eta_{\rm k} = 1$.

In hydroART, each grid cell records the hydrogen density and the type II and type Ia total mass fractions, $Z_{\rm II}$ and $Z_{\rm Ia}$. To compute the abundance fractions from Eq. 4, we require the individual mass fractions of hydrogen, helium, and the included metal species. For type II composition, we use the production factors from the rotating models of Chieffi & Limongi (2013). The production factors are determined by integrating the model yields for different mass progenitors across the Salpeter initial mass function ($\alpha = 2.35$, Salpeter 1955) over the progenitor mass range 13–120 $M_\odot$. For type Ia composition, we use the yields, $(Y_{\rm k}/Y_{\rm k\odot})/(Y_{\rm Fe}/Y_{\rm Fe\odot})$ from the C series DD2 models of Iwamoto et al. (1999), which are the most consistent with observational constraints of the nucleosynthesis products in the Galaxy.

We denote the type II and type Ia mass fractions for atomic species k as $(x_{\rm k})_{\rm II}$ and $(x_{\rm k})_{\rm Ia}$, respectively. For hydrogen and helium, $Y_1 = Y_2 = 0$, yielding $(x_1)_{\rm Ia} = (x_2)_{\rm Ia} = 0$. The metal mass fractions are rescaled by a constant to recover the mass fractions in the grid cell,

$$Z_{\rm II} = C_{\rm II}\sum_{\rm k=3}(x_{\rm k})_{\rm II}\,, \qquad Z_{\rm Ia} = C_{\rm Ia}\sum_{\rm k=3}(x_{\rm k})_{\rm Ia}\,. \quad (5)$$

For consistency, only the atomic species that are incorporated in the ionization model are included in the sums. We now need to rescale the hydrogen and helium mass fractions. Since all the hydrogen and helium originates from the type II ejecta[2], we define $r = (x_2)_{\rm II}/(x_1)_{\rm II}$, and obtain the mass fractions

[2] The grid cells are initially given the primordial hydrogen and helium mass fractions at $z = 50$, the starting redshift of the simulation. We do not apply a chemical evolution model to account for the full history of the grid cells, but assume that the feedback enrichment dominates.

for the mixture (employed in Eq. 4),

$$x_1 = \frac{1-(Z_{\rm II}+Z_{\rm Ia})}{1+r}\,, \quad x_2 = r x_1\,, \quad x_{\rm k} = C_{\rm II}(x_{\rm k})_{\rm II} + C_{\rm Ia}(x_{\rm k})_{\rm Ia}\,, \quad (6)$$

which preserves the constraint $\sum_{\rm k=1} x_{\rm k} = 1$.

If desired, solar abundance pattern can be used, in which case we directly employ the solar mass fractions from Table 1.4 of Draine (2011), which are derived from Asplund et al. (2009). Finally, the metallicity of the gas in solar units is

$$Z/Z_\odot = \frac{\sum\limits_{\rm k=3}(x_{\rm k}/x_{\rm H})}{\sum\limits_{\rm k=3}(x_{\rm k}/x_{\rm H})_\odot}\,, \quad (7)$$

where $x_{\rm H} = x_1$.

Since each ion k, j donates $j-1$ electrons to the free electron pool, the contribution to the electron density from each ion is $(j-1)n_{\rm k,j}$. The total electron density from all ions is then

$$n_{\rm e} = \sum_{\rm k}\sum_{\rm j=2}^{\rm k+1}(j-1)\,n_{\rm k,j}\,. \quad (8)$$

Introducing the ionization fractions, $f_{\rm k,j}(n_{\rm e},T,J_E) = n_{\rm k,j}/n_{\rm k}$, we write $n_{\rm k,j} = f_{\rm k,j}n_{\rm k} = f_{\rm k,j}\eta_{\rm k}n_{\rm A}$, and obtain the equation for charge density conservation,

$$n_{\rm e} = n_{\rm A}\sum_{\rm k}\eta_{\rm k}\sum_{\rm j=2}^{\rm k+1}(j-1)\,f_{\rm k,j}(n_{\rm e},T,J_E)\,. \quad (9)$$

Note that the ionization fraction depends upon the electron density, temperature, and the ionizing photon field, J_E. Eq. 9 is a linear transcendental equation; the electron density, $n_{\rm e}$, must be known in order to calculated the ionization fractions, which are constrained via particle and charge density conservation to yield a free electron pool with density $n_{\rm e}$.

3.3. *Ionizing Spectrum*

We provide the options (1) ionization by the ultraviolet background (UVB), which is redshift dependent, (2) ionization by stellar populations, which depends on each populations total stellar mass, age, metallicity, and distance from the model cloud, and (3) ionization by both the UVB and stellar populations.

For the UVB, we use the SEDs of Haardt & Madau (2011) added to the cosmic microwave background. These spectra are specified as the specific intensity, J_ν [erg s^{-1} cm^{-2} str^{-1} Hz^{-1}] over the energy [eV] interval $-6.7 \le \log E \le 6.8$ and are provided for redshifts $0 \le z \le 5$. Once the cloud redshift is specified, a grid of SEDS sampled at intervals of $\Delta z = 0.2$ are cubic spline interpolated at each frequency to obtain $J_\nu(z)$, which is then converted to the specific intensity per unit energy, $J_E(z)$ [cm^{-1} s^{-1} str^{-1}] versus E [eV] via $J_E\,dE = J_\nu\,d\nu$.

For the stellar populations, we use SEDs computed from the Starburst99 v6.02 models (Leitherer et al. 1999). We built a library of SEDs comprising stellar populations of $M = 10^3$, 10^4, 10^5, and 10^6 M$_\odot$. For each mass, five ages were computed (1, 5, 10, 20, and 40 Myr) and for each mass and age five metallicities were computed (10^{-4}, 10^{-3}, 10^{-2}, 10^{-1}, and 1 $Z_\odot$). We store the SEDs as the luminosity density per unit wavelength, L_λ [erg s^{-1} Å^{-1}] over the wavelength range $91 \le \lambda \le 1.6\times10^6$ Å, which corresponds to the energy [eV] interval $-2.1 \le \log E \le 2.1$.

Once the desired mass, age, and metallicity are specified, we first cubic spline interpolate L_λ at each wavelength across mass for each age and metallicity, then across age for each metallicity, and then across metallicity. The final SED is then converted to the flux density per unit wavelength, $F_\lambda = L_\lambda/(4\pi r^2)$ [erg s^{-1} cm^{-2} str^{-1} Å^{-1}], where r is the specified distance to the stellar population from the model cloud. Finally, we convert the SED to J_E versus E. If a combined UVB plus stellar population SED is used, the two specific intensities are added. In general, the contribution by stars scales linearly with the mass of the stellar population and with the inverse square of the distance between the model cloud and the stellar population.

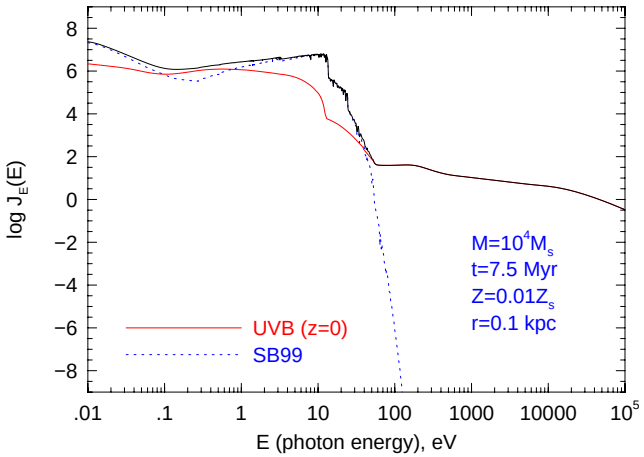

Figure 1. An example spectral energy distribution, J_E [cm^{-1} s^{-1} str^{-1}] versus E [eV]. The red curve is the Haardt & Madau (2011) UVB for $z = 0$. The blue dotted curve is the Starburst99 (Leitherer et al. 1999) model (SB99) for a single stellar population of mass 10^4 M$_\odot$ with age 7.5 Myr, and a metallicity of 0.01 in solar units. The black curve is the total of the two contributions. For this example, the the stellar population is assumed to be at a distance of 100 pc from the model cloud.

In Figure 1, we illustrate a SED that combines contributions from both the UVB (red curve) and a stellar population (blue dotted curve). For this example, the UVB is a $z = 0$ Haardt & Madau (2011) spectrum and the stellar population has mass $M_* = 10^4$ M$_\odot$, age $t = 7.5$ Myr, and metallicity $\log Z/Z_\odot = -1$ and is at a distance of 100 pc. There is no attenuation. Typical of this example, stellar radiation modifies the UVB SED in the spectral region below 100 eV, and when present, will generally lead to higher ionization conditions in regions where photoionization dominates. Even with no assumed attenuation through the ISM, stellar SEDs rarely modify the UVB incident on a grid cell unless the stellar population is very close in proximity, otherwise the population needs to be very young (populated with O stars) and massive (Churchill & Le Brun 1998).

3.4. *Ionization Rates*

We treat photoionizationa and Auger ionization (Section 3.4.1), direct collisional ionization (Section 3.4.2), and excitation auto-ionization processes (Section 3.4.3). We also treat charge exchange ionization, which is presented in Section 3.6.

3.4.1. *Photo and Auger Ionization*

Photoionization and Auger ionization both begin with radiative ionization processes in which a bound electron is photo-ejected from an ion or neutral atom. The electron can be liberated from any one of the ion's populated electron

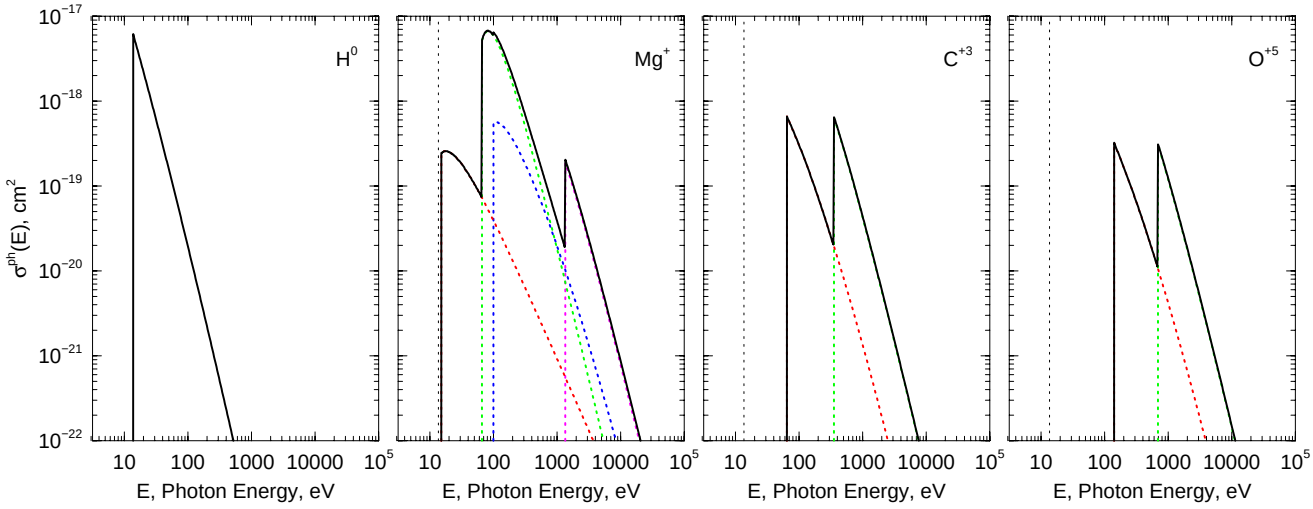

Figure 2. The photoionization cross sections [cm^2] for H^0, Mg$^+$, C^{+3}, and O^{+5} as a function of the photon energy [eV]. For H^0, the cross section is for the 1s shell. For Mg$^+$, the red curve is the 3s shell, the green curve is the 2p shell, the blue curve is the 2s shell, and the magenta curve is the 1s shell. For C^{+3} and O^{+5}, the red curve is the 2s shell and the green curve is the 1s shell. The total cross sections are given by the black curves. For reference, the vertical dotted line is the ground-state ionization energy for H^0.

shells.

To compute the rate, $R^{\rm ph}_{\rm k,j,s}$, at which an electron in a given shell, index s, is photo-ejected from ion k,j, we multiply the cross section for absorption, $\sigma^{\rm ph}_{\rm k,j,s}(E)$, for shell s at energy $E = h\nu$ by the photon number density per unit energy, $4\pi J_E/E$ [erg^{-1} cm^{-2} s^{-1}], and integrate over all energies greater than the binding energy of the electron,

$$R^{\rm ph}_{\rm k,j,s} = 4\pi \int_{I_{\rm k,j,s}}^{\infty} J_E \sigma^{\rm ph}_{\rm k,j,s}(E) \frac{dE}{E}, \qquad (10)$$

where $I_{\rm k,j,s}$ is the ionization (binding) energy for electrons in shell s of ion k,j.

For the computation of Eq. 10, we adopt the convention for the shell indices such that s = 1 is the 1s shell, s = 2 is 2s, s = 3 is 2p, s = 4 is 3s, s = 5 is 3p, s = 6 is 3d, and s = 7 is 4s. The photoionization cross sections are computed from the fitting functions and fitting parameters tabulated by Verner & Iakovlev (1995) for inner shells and by Verner et al. (1996) for the outer shells. Their work includes all ionization stages and shells for hydrogen through zinc. We computed $\sigma^{\rm ph}_{\rm k,j,s}(E)$ from,

$$\sigma^{\rm ph}_{\rm k,j,s}(E) = \sigma_0 y^{-Q} \frac{(x-1)^2 + y_{\rm W}^2}{[1+(y/y_{\rm A})^{1/2}]^P}, \qquad (11)$$

where $x = E/E_0 - y_0$ and $y = (x^2 + y_1^2)^{1/2}$. The tabulated fitting parameters for each k,j,s are σ_0, E_0, $y_{\rm A}$, P, $y_{\rm W}$, y_0, and y_1. For inner shells $y_{\rm W}$, y_0, and y_1 are null and the asymptotic power is $Q = \frac{1}{2}P + \ell + \frac{11}{2}$, where ℓ is the angular momentum quantum number of the shell. For the outer shell $Q = \frac{1}{2}P + \frac{11}{2}$. The physical interpretation of each fitting parameter is explained in Verner et al. (1996).

In Figure 2, we present the photoionization cross sections for H^0, and Mg$^+$, and C^{+3}, and O^{+5} as a function of the photon energy as computed from Eq. 11 and applied in Eq. 10. Ground-state Mg$^+$ has the isoelectronic sequence of neutral sodium ($1s^2 2s^2 2p^6 3s^1$) and ground-state C^{+3}, and O^{+5} have the isoelectronic sequence of neutral lithium ($1s^2 2s^1$). The individual shell cross sections are shown as colored dotted curves and the total is the solid curve. The red curves are the ground-state ionization threshold energies for the outermost populated electron shell.

In the case of photoionization, a single electron, $e^-_{\rm ej}$, is ejected and the ionization stage of the incident ion k,j is incremented by one to $k, j+1$,

$$A_{\rm k,j} + \gamma \rightarrow A_{\rm k,j+1} + e^-_{\rm ej}. \qquad (12)$$

In cases where the incident photon has the required energy to liberate an inner shell electron some of its energy can be channeled into also liberating one or more of the less bound, higher shell electrons. This process is known as Auger ionization, in which the ionization stage of the incident ion k,j is incremented by two or more,

$$A_{\rm k,j} + \gamma \rightarrow A_{\rm k,m} + (m-j)\, e^-_{\rm ej}, \qquad (13)$$

where we use the convention that that the initial ionization stage is j and the final higher ionization stage is m. Note that the number of ejected electrons is $N_{\rm e} = m - j$. Because the photo-electron is included in the notation, the final stage m is always greater than or equal to $j+2$. Photoionization is the special case in which $m = j+1$.

In order to compute the photo and Auger ionization rates, it is necessary to know the yield probability, $P^{\rm s}_{\rm k,j,m\text{-}j}$, i.e., the probability that $N_{\rm e} = m - j$ electrons in total are ejected from an ion following a photoionization of an electron originating from shell s (the photo-electron). These yield probabilities have been calculated and tabulated by Kaastra & Mewe (1993) for each electron shell.

For photoionization, the total photoionization rate, $R^{\rm ph}_{\rm k,j}$, for destruction of ion k,j is given by $R^{\rm ph}_{\rm k,j,s}$ (see Eq. 10), the rate at which an electron bound in shell s of ion k,j is ionized by incident photons, weighted by the probability that only the photo-electron is ejected from the ion and summed over all electron shells,

$$R^{\rm ph}_{\rm k,j} = \sum_{s=1}^{N^{\rm s}_{\rm k,j}} P^{\rm s}_{\rm k,j,1} R^{\rm ph}_{\rm k,j,s}, \qquad (14)$$

where $N^{\rm s}_{\rm k,j}$ is the number of shells for ion k,j.

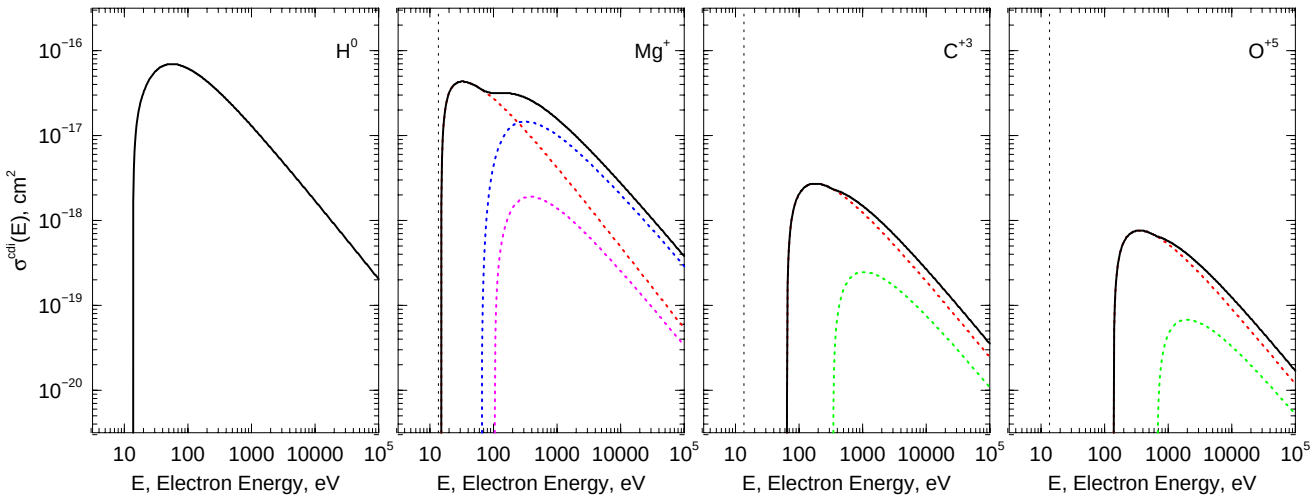

Figure 3. The direct collisional ionization cross sections [cm^2] for H^0, Mg^+, C^{+3}, and O^{+5} as a function of the electron energy [eV]. For H^0, the cross section is for the 1s shell. For Mg^+, the red curve is the 3s shell, the blue curve is the 2s+2p shell, and the magenta curve is the 1s shell. For C^{+3} and O^{+5}, the red curve is the 2s shell and the green curve is the 1s shell. The total cross sections are given by the black curves. For reference, the vertical dotted line is the ground-state ionization energy for H^0.

Similarly, the Auger ionization rate, $R^{\rm aug}_{{\rm k,j,m}}$, for destruction of an ion k,j that ejects $N_{\rm e} = m - j$ electrons (including the photo-electron, so $N_{\rm e} \geq 2$) is the sum of $R^{\rm ph}_{{\rm k,j,s}}$ over all electron shells weighted by the probability that $N_{\rm e}$ electrons in total were ejected from the ion in response to a photo-electron originating in shell s,

$$R^{\rm aug}_{{\rm k,j,m}} = \sum_{s=1}^{N^{\rm s}_{\rm k,j}} P^{\ {\rm s}}_{{\rm k,j,m-j}} R^{\rm ph}_{{\rm k,j,s}} \,. \tag{15}$$

The $R^{\rm aug}_{{\rm k,j,m}}$ are unique amongst the various ionization rates, because they dictate the balance between non-adjacent ionization stages of species k. Clearly, $R^{\rm aug}_{{\rm k,k+1,m}} = R^{\rm aug}_{{\rm k,k,m}} = 0$ since fully ionized and hydrogenic ions cannot undergo Auger ionization.

3.4.2. *Direct Collisional Ionization*

Direct collisional ionization is the collision of an electron with an ion, which then directly ionizes from j to $j+1$,

$$A_{\rm k,j} + {\rm e}^-_{\rm f} \rightarrow A_{\rm k,j+1} + {\rm e}^-_{\rm f} + {\rm e}^-_{\rm ej} \,. \tag{16}$$

In the process, the colliding free electron, e^-_f, loses an energy equal to the ionization energy plus the kinetic energy of the ejected electron.

The ionization rate for destruction of ion k,j due to direct collisional ionization is obtained by multiplying the total direct collisional ionization rate coefficient, $\alpha^{\rm cdi}_{\rm k,j}(T)$, by the number density of free electrons,

$$R^{\rm cdi}_{\rm k,j}(T) = n_{\rm e} \alpha^{\rm cdi}_{\rm k,j}(T) \,, \tag{17}$$

where

$$\alpha^{\rm cdi}_{\rm k,j}(T) = \sum_{s=1}^{N^{\rm s}_{\rm k,j}} \alpha^{\rm cdi}_{\rm k,j,s}(T) \,. \tag{18}$$

is the sum of the direct collisional ionization rate coefficient contributions, $\alpha^{\rm cdi}_{\rm k,j,s}(T)$, for ejection of an electron from shell s. Here, the shell indices are $s = 1$ is the 1s shell, $s = 2$ is the combined 2s+2p shell, $s = 3$ is the combined 3s+3p shell, and $s = 4$ is the 4s shell.

The $\alpha^{\rm cdi}_{\rm k,j,s}(T)$ are the expectation values $\left\langle \sigma^{\rm cdi}_{\rm k,j,s} \cdot v \right\rangle$, where $\sigma^{\rm cdi}_{\rm k,j,s}(E)$ is the direct collisional ionization cross section for the shell, $v(E) = \sqrt{2kE/m_{\rm e}}$ is the electron speed for kinetic energy E, and $m_{\rm e}$ is the electron mass. The integration is over energies large enough to overcome the binding energy,

$$\begin{aligned} \alpha^{\rm cdi}_{\rm k,j,s}(T) &= \left\langle \sigma^{\rm cdi}_{\rm k,j,s} \cdot v \right\rangle \\ &= \sqrt{\frac{2k}{m_{\rm e}}} \int_{I_{\rm k,j,s}}^{\infty} \sigma^{\rm cdi}_{\rm k,j,s}(E) f(E,T) E^{1/2} dE \,, \end{aligned} \tag{19}$$

where $f(E,T)$ is the Maxwell-Boltzmann speed distribution function at equilibrium temperature T, and $I_{\rm k,j,s}$ is the ionization energy of shell s of ion $k,j,$.

The direct collisional ionization cross sections and rate coefficients are computed from the fitting functions and parameters tabulated by Arnaud & Rothenflung (1985). For shell s of ion k,j, let $u_1 = E/I_{\rm k,j,s}$ and $u_2 = 1 - I_{\rm k,j,s}/E$. The direct collisional ionization cross section for shell s is computed from

$$\sigma^{\rm cdi}_{\rm k,j,s}(E) = \frac{10^{-14}}{u_1 I^2_{\rm k,j,s}} \left\{ a^{\rm s}_{\rm k,j} u_2 + b^{\rm s}_{\rm k,j} u_2^2 + c^{\rm s}_{\rm k,j} \ln u_1 + d^{\rm s}_{\rm k,j} \frac{\ln u_1}{u_1} \right\} , \tag{20}$$

where the four fitting coefficients, $a^{\rm s}_{\rm k,j}$, $b^{\rm s}_{\rm k,j}$, $c^{\rm s}_{\rm k,j}$, and $d^{\rm s}_{\rm k,j}$, are tabulated in Arnaud & Rothenflung (1985) for each shell for all ion stages of hydrogen through nickel. The units of the fitting coefficients are 10^{-14} cm^2 eV^2. In Figure 3, we present the direct collisional ionization cross sections for H^0, and Mg^+, and C^{+3}, and O^{+5} as a function of the electron energy as computed from Eq. 20. The individual shell cross sections are shown as colored dotted curves. The red curves are the ground-state ionization threshold energies for the outermost populated electron shell.

Rather than integrate Eq. 19 using Eq. 20, which can be computationally expensive, we computed $\alpha^{\rm cdi}_{\rm k,j,s}(T)$ for each shell using the fitting formulae of Arnaud & Rothenflung (1985), for which the same fitting coefficients employed for the cross sections apply. Let $x^{\rm s}_{\rm k,j} = I_{\rm k,j,s}/kT$, then

$$\alpha^{\rm cdi}_{\rm k,j,s}(T) = \frac{6.69 \times 10^{-7}}{(kT)^{3/2}} F^{\rm s}_{\rm k,j}(x^{\rm s}_{\rm k,j}) \frac{\exp\left\{-x^{\rm s}_{\rm k,j}\right\}}{x^{\rm s}_{\rm k,j}} \,, \tag{21}$$

where

$$F^{s}_{k,j}(x) = a^{s}_{k,j}\left[1-xf_1(x)\right] + b^{s}_{k,j}\left[1+x-x(2+x)f_1(x)\right] + c^{s}_{k,j}f_1(x) + d^{s}_{k,j}xf_2(x) \quad (22)$$

and where

$$f_1(x) = e^x\int_1^\infty \frac{dt}{t}e^{-xt} \qquad f_2(x) = e^x\int_1^\infty \frac{dt}{t}e^{-xt}\ln t\,. \quad (23)$$

The integral for $f_1(x)$ is the well known Exponential function. Both $f_1(x)$ and $f_2(x)$ are computed from the closed form formulae given in Arnaud & Rothenflung (1985), incorporating the corrections given by Verner & Iakovlev (1990). We then compute the total direct collisional ionization rate coefficient, $\alpha^{cdi}_{k,j}(T)$, for ion k,j using Eq. 18. We also examined the rate coefficient formulae and parameters of Voronov (1997), but found the results comparable.

3.4.3. *Excitation-Auto Ionization*

Excitation auto-ionization (E-A) occurs in ions with many inner filled shell electrons and only a few outer shell electrons. A collision with a free electron first excites the ion. Then, during the internal de-excitation process the released energy can either channel into recombination emission lines or into liberating an outer shell electron, which is auto-ionization,

$$A_{k,j} + e^-_f \rightarrow A^*_{k,j} + e^-_f \rightarrow A_{k,j+1} + e^-_{ej} + e^-_f\,, \quad (24)$$

where e^-_f the free collisional electron and the e^-_{ej} is ejected auto-ionized electron.

The ionization rate for destruction of ion k,j due to E-A collisional ionization is obtained by multiplying the E-A collisional ionization rate coefficient, $\alpha^{cea}_{k,j}(T)$, by the number density of free electrons,

$$R^{cea}_{k,j}(T) = n_e\alpha^{cea}_{k,j}(T)\,. \quad (25)$$

The total E-A rate coefficient is given by the expectation value $\alpha^{cea}_{k,j}(T) = \left\langle \sigma^{cea}_{k,j}\cdot v\right\rangle$ computed from Eq. 19 with $I_{k,j,s}$ replaced by $\chi_{k,j}$, the E-A onset energy and $\sigma^{cdi}_{k,j,s}(E)$ replaced by $\sigma^{cea}_{k,j}(E)$, the total E-A cross section, which is obtained by weighting the de-excitation transition channels over all transitions.

The E-A cross sections and rate coefficients depend on the bound electron configuration of the ion, i.e., the isoelectronic sequence. For example, C^{+3}, N^{+4}, and O^{+5} all have the electron configuration of neutral lithium ($1s^2 2s$) and are thus lithium isosequence ions ($N_e = 3$).

There is no E-A process for hydrogen and helium sequence ions. For lithium sequence ions, the dominant contribution to the cross section is the 1s–2p transition. As the charge of the ion, Z, increases, the branching ratio to E-A decreases. No significant E-A contribution to the direct collisional cross section is observed for the beryllium sequence (except perhaps O^{+4}, which is neglected), nor for the sequences from boron to neon, which differ only in the number of 2p shell electrons. For the sodium sequence ($[Ne]3s^1$), up to 18 transitions can contribute to E-A, for which the relative importance increases with Z. The sequences from magnesium to argon differ in the number of 3p shell electrons, and the relative importance of E-A decreases as the shell fills.

We computed the total E-A cross sections and rate coefficients for ions up to nickel using the fitting functions and parameters tabulated by Arnaud & Rothenflung (1985),

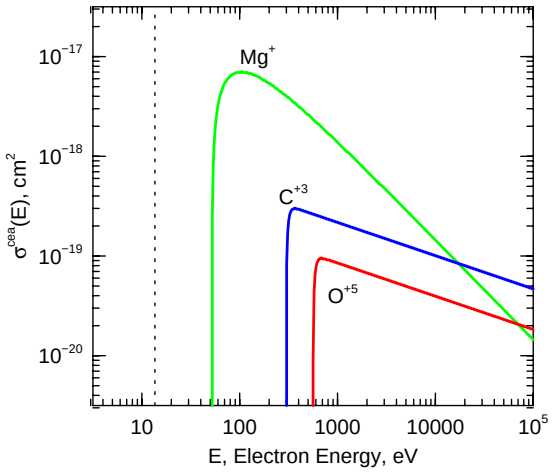

Figure 4. The excitation auto-ionization collisional cross sections [cm^2] for Mg^+, C^{+3}, and O^{+5} as a function of the electron energy [eV]. For H^0, the cross section is null. Mg^+ is shown as the green curve, C^{+3} as the blue curve, and O^{+5} as the red curve. For reference, the vertical dotted line is the ground-state ionization energy for H^0.

with the exceptions of the iron ions, which are computed from the fitting functions and parameters updated by Arnaud & Raymond (1992), and the cross sections for the lithium sequence, which we obtained from Hu et al. (1996).

In order to simplify the individually presented fitting functions of Arnaud & Rothenflung (1985) and Hu et al. (1996), we present uniformly generalized fitting functions for which we have distilled several of the their fitting parameters into fewer terms. For ion k,j, the total E-A cross section is computed from

$$\sigma^{cea}_{k,j}(E) = \frac{\sigma_0}{Z^2_{eff}}\frac{1}{u^a_{k,j}}\left(1-\frac{1}{u^n_{k,j}}\right)\,, \quad (26)$$

where $u_{k,j} = E/\chi_{k,j}$, and where E is the incident electron kinetic energy. The range of applicable Z, and the fitting parameters, $\chi_{k,j}$, Z_{eff}, σ_0, a, and n are listed in upper panel of Table 1 as a function of isoelectronic sequence, given by N_e. The translation between isoelectronic sequence and the ion index k,j is given by $N_e = k-j+1$. Four special cases are treated, for which the fitting function takes the form

$$\sigma^{cea}_{k,j}(E) = \frac{\sigma_0}{u_{k,j}}\left(1-a\ln u_{k,j}\right)\,, \quad (27)$$

and for which the fitting parameters are listed in the lower panel of Table 1. In Figure 4, we present the E-A cross sections for Mg^+ (green curve), C^{+3} (blue curve), and O^{+5} (red curve) as a function of the electron energy as computed from Eq. 26.

For ion k,j, the total E-A rate coefficients are computed from

$$\alpha^{cea}_{k,j}(T) = \frac{\alpha_0}{Z^2_{eff}(1+b)}\frac{G_{iso}(x_{k,j})}{(kT)^{1/2}}\exp\{-x_{k,j}\}\,, \quad (28)$$

where $x_{k,j} = \chi_{k,j}/kT$, and

$$G_{iso}(x) = \sum_{n=0}^{3} a_n x^n + f_1(x)\sum_{n=0}^{3} a_{n+4}x^n\,, \quad (29)$$

where $f_1(x)$ is given by Eq. 23. The fitting parameters, Z_{eff}, α_0, b, and coefficients a_n for $G_{iso}(x)$ are listed in Table 2. Note that the range of applicable Z and the ionization potentials used in Eq. 28 are listed in Table 1.

Table 1
Fitting Parameters for Excitation-Autoionization Cross Sections[a]

Sequence	N_e	Z Range	$\chi_{k,j}$ [eV]	Z_{eff}	σ_0 [cm^2]	a	n
[He]2s^1 Li[b]	3	4–28	$13.6\{(Z-0.835)^2+(Z-1.62)^2\}$	Z^2	4.22×10^{-16}	1/3	20
[Ne]3s^1 Na (low Z)	11	12–16	$26.0(Z-10)$	$(Z-11)^{0.35}$	2.8×10^{-17}	1	1
[Ne]3s^1 Na (high Z)	11	18–28	$11.0(Z-10)^{1.50}$	$(Z-10)^{1.87}$	1.3×10^{-14}	1	3
[Ne]3s^2 Mg	12	18–28	$10.3(Z-10)^{1.52}$	Z	$4.0\times10^{-13}/\chi_{k,j}$	1	3
[Ne]3p^1 Al	13	18–28	$18.0(Z-11)^{1.33}$	Z	$4.0\times10^{-13}/\chi_{k,j}$	1	3
[Ne]3p^2 Si	14	18–28	$18.4(Z-12)^{1.36}$	Z	$4.0\times10^{-13}/\chi_{k,j}$	1	3
[Ne]3p^3 P	15	18–28	$23.7(Z-13)^{1.29}$	Z	$4.0\times10^{-13}/\chi_{k,j}$	1	3
[Ne]3p^4 S	16	18–28	$40.0(Z-14)^{1.10}$	Z	$4.0\times10^{-13}/\chi_{k,j}$	1	3
Special Cases							
[Ar]4s^2 Ca^0	20	20	25.0	⋯	6.0×10^{-17}	1.12	⋯
[Ar]4s^1 Ca$^+$	19	20	29.0	⋯	9.8×10^{-17}	1.12	⋯
[Ar]3d^{3}4s^2 Fe^{+3}	23	26	60.0	⋯	1.8×10^{-17}	1.0	⋯
[Ar]3d^{2}4s^2 Fe^{+4}	22	26	73.0	⋯	5.0×10^{-18}	1.0	⋯

[a] The connection between isoelectronic series and index k, j is $N_e = k-j+1$ and $Z = k$.
[b] The fitting parameters for lithium are taken from Hu et al. (1996).

Table 2
Fitting Parameters for Excitation-Autoionization Rate Coefficients[a]

Sequence	Z_{eff}	α_0 [cm^3 s^{-1} eV$^{1/2}$]	b	$G_{iso}(x): a_0;a_1;a_2;a_3;a_4;a_5;a_6;a_7$
[He]2s^1 Li[b]	$(Z-0.43)$	1.600×10^{-7}	$0.0002Z^3$	0.67; 1.20; 0; 0; 2.22; –0.18; –1.20; 0
[Ne]3s^1 Na (low Z)	$(Z-11)^{0.35}$	$1.873\times10^{-9}/\chi_{k,j}$	0	1.00; 0; 0; 0; 0; –1.00; 0, 0
[Ne]3s^1 Na (high Z)	$(Z-10)^{1.87}$	$8.697\times10^{-7}/\chi_{k,j}$	0	1.00; –0.50; 0.50; 0; 0; 0; 0; –0.50
[Ne]3s^2 Mg	Z	2.676×10^{-5}	0	1.00; –0.50; 0.50; 0; 0; 0; 0; –0.50
[Ne]3p^1 Al	Z	2.676×10^{-5}	0	1.00; –0.50; 0.50; 0; 0; 0; 0; –0.50
[Ne]3p^2 Si	Z	2.676×10^{-5}	0	1.00; –0.50; 0.50; 0; 0; 0; 0; –0.50
[Ne]3p^3 P	Z	2.676×10^{-5}	0	1.00; –0.50; 0.50; 0; 0; 0; 0; –0.50
[Ne]3p^4 S	Z	2.676×10^{-5}	0	1.00; –0.50; 0.50; 0; 0; 0; 0; –0.50
Special Cases				
[Ar]4s^2 Ca^0	1.0	$4.014\times10^{-9}/\chi_{k,j}$	0	1.00; 0; 0; 0; 1.12; 0; 0; 0
[Ar]4s^1 Ca$^+$	1.0	$6.556\times10^{-9}/\chi_{k,j}$	0	1.00; 0; 0; 0; 1.12; 0; 0; 0
[Ar]3d^{3}4s^2 Fe^{+3}	1.0	$1.204\times10^{-9}/\chi_{k,j}$	0	1.00; 0; 0; 0; 1.00; 0; 0; 0
[Ar]3d^{2}4s^2 Fe^{+4}	1.0	$3.345\times10^{-9}/\chi_{k,j}$	0	1.00; 0; 0; 0; –1.00; 0; 0; 0

[a] The connection between isoelectronic series and index k, j is $N_e = k-j+1$ and $Z = k$.
[b] The tabulated value of α_0 for the lithium sequence requires an additional multiplicative term. For C^{+3}, multiply by 0.6. For N^{+4}, multiply by 0.8. For O^{+5}, multiply by 1.25. For all other ions, multiply by 1.2.

3.5. *Recombination Rates*

We treat radiative recombination (Section 3.5.1) and dielectronic recombination (Section 3.5.2). Charge exchange recombination is discussed in Section 3.6.

3.5.1. *Radiative Recombination*

Radiative recombination is the capture of a free electron by ion $k, j+1$ followed by the emission of a photon,

$$A_{k,j+1} + e_f^- \rightarrow A_{k,j} + \gamma\,. \tag{30}$$

The radiative recombination rate for creation of ion k, j due to electron recombination with ion $k, j+1$ is obtained by multiplying the total recombination rate coefficient, $\beta_{k,j}^{phr}(T)$, by the electron number density,

$$R_{k,j+1}^{phr}(T) = n_e \beta_{k,j}^{phr}(T)\,. \tag{31}$$

The cross section for capture of a free electron decreases with electron kinetic energy. Given the cross section, $\sigma_{k,j,s}^{phr}(E)$, for radiative recombination to shell s forming ion k, j, the radiative recombination rate coefficient for the shell, $\beta_{k,j,s}^{phr}(T)$, is obtained by integrating over all electron velocities, analogous to Eq. 19, i.e., with no threshold energy ($I_{k,j,s} \rightarrow 0$) and with $\sigma_{k,j,s}^{cdi}(E)$ replaced by $\sigma_{k,j,s}^{phr}(E)$. We have ignored radiation induced recombination. The total recombination rate coefficient is the sum over all shells,

$$\beta_{k,j}^{phr}(T) = \sum_{s=1}^{N_{k,j}^s} \beta_{k,j,s}^{phr}(T)\,. \tag{32}$$

For hydrogenic ions (N_e = 1) we use the formula originally proposed by Seaton (1959), which is highly accurate (Arnaud & Rothenflug 1985; Dopita & Sutherland 2003),

$$\beta_{k,j}^{phr}(T) = \beta_0 Z_k \lambda^{1/2}\left[0.4288 + 0.5\ln\lambda + 0.469\lambda^{-1/3}\right]\,, \tag{33}$$

where $\beta_0 = 5.197\times10^{-14}$ and where $\lambda = Z_k^2(1.5789\times10^5/T)$.

The Atomic and Molecular Diagnostic Processes in Plasmas (AMDPP) group has published fitting functions and parameters for radiative recombination rate coefficients for many non-hydrogenic ions (Badnell 2006). The functional

form is

$$\beta_{\rm k,j}^{\rm phr}(T) = \frac{a_{\rm k,j}}{\left(T/t_{\rm k,j}^{(0)}\right)^{1/2}} \frac{\left[1+\left(T/t_{\rm k,j}^{(0)}\right)^{1/2}\right]^{b'_{\rm k,j}-1}}{\left[1+\left(T/t_{\rm k,j}^{(1)}\right)^{1/2}\right]^{b'_{\rm k,j}+1}}\,, \tag{34}$$

where $a_{\rm k,j}$, $t_{\rm k,j}^{(0)}$, $t_{\rm k,j}^{(1)}$ are tabulated fitting parameters, and $b'_{\rm k,j} = b_{\rm k,j} + c_{\rm k,j}\exp\{-t_{\rm k,j}^{(2)}/T\}$, where $b_{\rm k,j}$, $c_{\rm k,j}$ and $t_{\rm k,j}^{(2)}$ are additional fitting parameters. Data are tabulated for all elements from helium to zinc for isoelectronic sequences up to the magnesium sequence ([Ne]3s^2, $N_{\rm e} = 12$). The fitting functions neglect narrow resonant spikes.

Since not all ionization stages have been tabulated by Badnell (2006), we employed the fitting functions and parameters for the simple power-law form published by Arnaud & Rothenflung (1985), based upon work of Seaton (1959), Aldrovandi & Pequignot (1973), and Shull & Van Steenberg (1982) for cases omitted from the AMDPP tables. The expression is

$$\beta_{\rm k,j}^{\rm phr}(T) = a_{\rm k,j} T_4^{-b_{\rm k,j}}\,, \tag{35}$$

where $T_4 = T/10^4$, and where $a_{\rm k,j}$ and $b_{\rm k,j}$ are the fitting parameters tabulated by Arnaud & Rothenflung (1985) for all ions of helium through nickel.

3.5.2. *Dielectronic Recombination*

Dielectronic recombination often dominates over radiative recombination. In this process, a high energy free electron first excites a bound deep inner shell electron prior to its capture in an elevated excited state of the ion. There are now two excited electrons and an unfilled state in an inner shell. Multiple channels of relaxation for the ion are now available (of which one is also auto-ionization).

In dielectronic recombination, the doubly excited ion works its way back to the ground state via multiple radiative cascades. At high temperatures this process usually proceeds first by the decay of one of the excited electrons to refill the empty inner shell by radiative decay followed by a downward cascade of the remaining excited electron. At low temperatures, the dominant channel occurs when the free electron is capture in a shell that is a resonant state to the emptied inner shell. The electron transitions rapidly and is then followed by a downward cascade of the remaining excited electron. The reaction can be written

$$A_{\rm k,j+1} + {\rm e}_{\rm f}^- \rightarrow A_{\rm k,j}^{**} \rightarrow A_{\rm k,j}^{*} + \gamma \rightarrow A_{\rm k,j+1} + \sum \gamma_i\,, \tag{36}$$

where the sum indicates that several recombination photons can be emitted during the cascade process.

The dielectronic recombination rate for creation of ion k, j due to electron recombination with ion $k, j+1$ is obtained by multiplying the total dielectronic recombination rate coefficient, $\beta_{\rm k,j}^{\rm die}(T)$, by the electron number density,

$$R_{\rm k,j+1}^{\rm die}(T) = n_{\rm e}\beta_{\rm k,j}^{\rm die}(T)\,. \tag{37}$$

Since the dominant channels for dielectronic recombination are temperature dependent, the rate coefficient is double peaked. For this reason, previous fitting functions and parameters for the rate coefficients were split into a low temperature regime (Nussbaumer & Storey 1983, 1986, 1987) and high temperature regime (Aldrovandi & Pequignot 1973; Shull & Van Steenberg 1982; Arnaud & Rothenflung 1985).

A newer fitting function and accompanying parameter list for all elements from helium to zinc and valid for temperatures ranging from $T \simeq 100$ to $T \simeq 10^7$K has been made available by the AMDPP group. We used the fitting functions and parameters described in Altun et al. (2007), which are based upon a series of papers (see references in Badnell et al. 2003; Altun et al. 2007). The fitting function has the form

$$\beta_{\rm k,j}^{\rm die}(T) = T^{-3/2}\sum_{i=1}^{N_{\rm k,j}} c_{\rm k,j,i}\exp\left\{-\frac{t_{\rm k,j,i}}{T}\right\}\,, \tag{38}$$

where $N_{\rm k,j}$ is the number of fitting parameters for ion k, j, and $c_{\rm k,j,i}$ and $t_{\rm k,j,i}$ are the fitting parameters.

3.6. *Charge Exchange*

Charge exchange is the transfer of an electron from one ion to another during a collision. Since hydrogen is the most abundant species, a charge exchange with a given metal ion k, j is dominated either by ionization ($k, j \rightarrow k, j+1$) from an ionized hydrogen (in which the H$^+$ ion recombines with the exchanged electron), or by recombination ($k, j-1 \rightarrow k, j$) via the ionization of neutral hydrogen,

$$A_{\rm k,j} + {\rm H}^+ \leftrightarrow A_{\rm k,j+1} + {\rm H}^0\,. \tag{39}$$

Helium is also relatively abundant and is the second most important charge exchange channel,

$$A_{\rm k,j+1} + {\rm He}^0 \leftrightarrow A_{\rm k,j} + {\rm He}^+\,. \tag{40}$$

The rate for destruction of ion k, j via charge exchange ionization with ionized hydrogen ($k = 1, j = 2$) is

$$R_{\rm k,j}^{\rm xH^+}(T) = n_{1,2}\alpha_{\rm k,j}^{\rm xH^+}(T)\,, \tag{41}$$

where $\alpha_{\rm k,j}^{\rm xH^+}(T)$ is the ionization rate coefficient. The rates for creation of ion $k, j-1$ via destruction of ion k, j via charge exchange recombination with neutral hydrogen ($k = 1, j = 1$) and with neutral helium ($k = 2, j = 1$) are given by

$$\begin{aligned} R_{\rm k,j}^{\rm xH}(T) &= n_{1,1}\beta_{\rm k,j\text{-}1}^{\rm xH}(T) \\ R_{\rm k,j}^{\rm xHe}(T) &= n_{2,1}\beta_{\rm k,j\text{-}1}^{\rm xHe}(T)\,, \end{aligned} \tag{42}$$

where $\beta_{\rm k,j\text{-}1}^{\rm xH}(T)$ and $\beta_{\rm k,j\text{-}1}^{\rm xHe}(T)$ are the respective recombination rate coefficients.

We computed the total charge exchange ionization and recombination rate coefficients using the fitting function and parameters of Kingdon & Ferland (1996). The rate coefficient for recombination to ion k, j via charge exchange from neutral hydrogen is given by

$$\beta_{\rm k,j}^{\rm xH}(T) = 10^{-9} a_{\rm k,j} T_4^{b_{\rm k,j}}\left[1 + c_{\rm k,j}\exp\{d_{\rm k,j}T_4\}\right]\,, \tag{43}$$

where $T_4 = T/10^4$, and where $a_{\rm k,j}$, $b_{\rm k,j}$, $c_{\rm k,j}$, and $d_{\rm k,j}$ are the fitting parameters. The rate coefficient for ionization of ion k, j via charge exchange to neutral hydrogen is obtained via detailed balancing,

$$\alpha_{\rm k,j}^{\rm xH^+}(T) = \beta_{\rm k,j}^{\rm xH}(T)\exp\left\{-\frac{\Delta E_{\rm k,j}}{kT_4}\right\}\,, \tag{44}$$

where the Boltzmann factor, $\Delta E_{\rm k,j}/k$, is also tabulated by Kingdon & Ferland (1996).

The computation of the recombination rate coefficient for charge exchange with neutral helium, $\beta_{\rm k,j}^{\rm xHe}(T)$, is also obtained from Eq. 43 using the parameters applicable to these reactions. The charge exchange ionization of metals via ionized

helium is not treated because, to date, there is not a uniform set of published rates covering a wide range of ions.

The fitting parameters provided by Kingdon & Ferland (1996) are presented for all species up to and including zinc, but only for the first three ionization stages. For ions with $j \geq 4$, we use the asymptotic formulae of Ferland, Korista, & Verner (1997),

$$\beta^{\rm xH}_{\rm k,j}(T) = 1.92 \times 10^{-9} Z_{\rm k} \,, \tag{45}$$

for hydrogen, and

$$\beta^{\rm xHe}_{\rm k,j}(T) = 5.4 \times 10^{-10} Z_{\rm k} \,, \tag{46}$$

for helium. The different constants are due to the different reduced masses of hydrogen and helium.

3.7. *Rate Equations*

Here, we derive the rate equations, $dn_{\rm k,j}/dt$, for all ionization stages of all treatable species. We assume two-level atoms, effectively the ground state and the continuum[3].

For the following, we drop the explicit temperature dependence of all rates and rate coefficients. We remind the reader that for recombination, the rate coefficients, $\beta_{\rm k,j}$, are indexed to the final state. However, we use the convention that all rates, $R_{\rm k,j}$, are indexed by the initial state.

3.7.1. *Hydrogen*

Hydrogen is the simplest case because the channels for creation and destruction involve only two adjacent ionization stages. Because of this, the hydrogen rate equations for $n_{1,1}$ and $n_{1,2}$ are antisymmetric,

$$\begin{aligned} \frac{dn_{1,1}}{dt} &= n_{1,2}\left(R^{\rm rec}_{1,2} + R^{\rm xH^+}_{1,2}\right) - n_{1,1}\left(R^{\rm ph}_{1,1} + R^{\rm coll}_{1,1} + R^{\rm xH}_{1,1}\right) \\ \frac{dn_{1,2}}{dt} &= -\frac{dn_{1,1}}{dt} \,. \end{aligned} \tag{47}$$

The creation rates of $n_{1,1}$ are due to the recombination of $n_{1,2}$ with free electrons, $R^{\rm rec}_{1,2}$, and ionization charge exchange from metals, $R^{\rm xH^+}_{1,2}$, where

$$\begin{aligned} R^{\rm rec}_{1,2} &= n_{\rm e}\beta^{\rm phr}_{1,1} \\ R^{\rm xH^+}_{1,2} &= \sum_{\rm k=2}^{\rm k}\sum_{\rm j=1} n_{\rm k,j}\alpha^{\rm xH^+}_{\rm k,j} \,. \end{aligned} \tag{48}$$

The destruction rates of $n_{1,1}$ are due to photoionization, $R^{\rm ph}_{1,1}$, collisional ionization via free electrons, $R^{\rm coll}_{1,1}$, and recombination charge exchange to metals, $R^{\rm xH}_{1,1}$, which ionizes neutral hydrogen, where

$$\begin{aligned} R^{\rm coll}_{1,1} &= n_{\rm e}\alpha^{\rm cdi}_{1,1} \\ R^{\rm xH}_{1,1} &= \sum_{\rm k=2}^{\rm k+1}\sum_{\rm j=2} n_{\rm k,j}\beta^{\rm xH}_{\rm k,j-1} \,. \end{aligned} \tag{49}$$

Note that the negative of these rates are also the destruction and creation rates of $n_{1,2}$, respectively.

3.7.2. *Helium*

Helium has three ionization stages. There is no published Auger channel directly connecting the neutral and fully ionized stages; however, non-zero dielectronic rate coefficients for the channel from singly ionized to neutral helium exist. The rate equation for neutral helium is

$$\frac{dn_{2,1}}{dt} = n_{2,2}\left(R^{\rm rec}_{2,2} + R^{\rm xHe^+}_{2,2}\right) - n_{2,1}\left(R^{\rm ph}_{2,1} + R^{\rm coll}_{2,1} + R^{\rm xHe}_{2,1}\right) \,. \tag{50}$$

The creation rates of $n_{2,1}$ are due to the recombination channels of $n_{2,2}$ with free electrons, $R^{\rm rec}_{2,2}$, and ionization charge exchange from metals, $R^{\rm xHe^+}_{2,2}$, where

$$\begin{aligned} R^{\rm rec}_{2,2} &= n_{\rm e}\left(\beta^{\rm phr}_{2,1} + \beta^{\rm die}_{2,1}\right) \\ R^{\rm xHe^+}_{2,2} &= n_{1,1}\alpha^{\rm xHe^+}_{1,1} + \sum_{\rm k=3}^{\rm k}\sum_{\rm j=1} n_{\rm k,j}\alpha^{\rm xHe^+}_{\rm k,j} \,. \end{aligned} \tag{51}$$

Recall, however, that we do not treat charge exchange ionization from ionized helium, so $R^{\rm xHe^+}_{2,2} = 0$ for our work.

The destruction rates of $n_{2,1}$ are due to photoionization, $R^{\rm ph}_{2,1}$, collisional ionization via free electrons, $R^{\rm coll}_{2,1}$, and recombination charge exchange to metals, $R^{\rm xH}_{2,1}$, which singly ionizes neutral helium, where

$$\begin{aligned} R^{\rm coll}_{2,1} &= n_{\rm e}\alpha^{\rm cdi}_{2,1} \\ R^{\rm xHe}_{2,1} &= n_{1,2}\beta^{\rm xHe}_{1,1} + \sum_{\rm k=3}^{\rm k+1}\sum_{\rm j=2} n_{\rm k,j}\beta^{\rm xHe}_{\rm k,j-1} \,, \end{aligned} \tag{52}$$

respectively. For twice ionized helium, the rate equation is

$$\frac{dn_{2,3}}{dt} = n_{2,2}\left(R^{\rm ph}_{2,2} + R^{\rm coll}_{2,2} + R^{\rm xH^+}_{2,2}\right) - n_{2,3}\left(R^{\rm rec}_{2,3} + R^{\rm xH}_{2,3}\right) \,. \tag{53}$$

The creation rates via the destruction of $n_{2,2}$ are due to photoionization, $R^{\rm ph}_{2,2}$, collisional ionization, $R^{\rm coll}_{2,2}$, and ionization via charge exchange recombination to ionized hydrogen, where

$$\begin{aligned} R^{\rm coll}_{2,2} &= n_{\rm e}\alpha^{\rm cdi}_{2,2} \\ R^{\rm xH^+}_{2,2} &= n_{1,2}\alpha^{\rm xH^+}_{2,2} \,. \end{aligned} \tag{54}$$

The destruction rates of $n_{2,3}$ are due to the channels of recombination with free electrons, $R^{\rm rec}_{2,3}$, and recombination via charge exchange ionization of neutral hydrogen, where

$$\begin{aligned} R^{\rm rec}_{2,3} &= n_{\rm e}\beta^{\rm phr}_{2,2} \\ R^{\rm xH}_{2,3} &= n_{1,1}\beta^{\rm xH}_{2,2} \,. \end{aligned} \tag{55}$$

For singly ionized helium, the creation and destruction rates are simply the negative of the sum of those for neutral and doubly ionized helium,

$$\frac{dn_{2,2}}{dt} = -\left(\frac{dn_{2,1}}{dt} + \frac{dn_{2,3}}{dt}\right) \,. \tag{56}$$

3.7.3. *Metals*

Here, we write out the rate equations for all ions with $k \geq 3$. For what follows, let $R^{\rm ion}_{\rm k,j-1}$ denote the creation rate of $n_{\rm k,j}$ via ionization of $n_{\rm k,j-1}$ and let $R^{\rm rec}_{\rm k,j+1}$ denote the creation rate of $n_{\rm k,j}$ via recombination from initial state $n_{\rm k,j+1}$. Further, let $R^{\rm rec}_{\rm k,j}$ denote the destruction rate of $n_{\rm k,j}$ via recombination to final state $n_{\rm k,j-1}$ and let $R^{\rm ion}_{\rm k,j}$ denote the destruction of $n_{\rm k,j}$ via ionization to final state $n_{\rm k,j+1}$. We then write

$$\begin{aligned} \frac{dn_{\rm k,j}}{dt} \;=\; & n_{\rm k,j-1}R^{\rm ion}_{\rm k,j-1} + n_{\rm k,j+1}R^{\rm rec}_{\rm k,j+1} + \sum_{\rm i=1}^{\rm j-2} n_{\rm k,i}R^{\rm aug}_{\rm k,i,j} \\ & - n_{\rm k,j}\left(R^{\rm ion}_{\rm k,j} + R^{\rm rec}_{\rm k,j} + \sum_{\rm m=j+2}^{\rm k-1} R^{\rm aug}_{\rm k,j,m}\right) \,. \end{aligned} \tag{57}$$

[3] For a brief discussion of the ramification of this assumption, see Section 11.1 of *Hazy 2* (Ferland 2002).

The creation rate of $n_{k,j}$ via ionization destruction of adjacent ion $n_{k,j-1}$ is

$$R^{\rm ion}_{k,j-1} = R^{\rm ph}_{k,j-1} + n_e\left(\alpha^{\rm cdi}_{k,j-1} + \alpha^{\rm cea}_{k,j-1}\right) + n_{1,2}\alpha^{\rm xH^+}_{k,j-1}\,. \tag{58}$$

Note that we do not treat charge exchange ionization from ionized helium. The creation rate of $n_{k,j}$ via recombination destruction of adjacent ion $n_{k,j+1}$ is

$$R^{\rm rec}_{k,j+1} = n_e\left(\beta^{\rm phr}_{k,j} + \beta^{\rm die}_{k,j}\right) + n_{1,1}\beta^{\rm xH}_{k,j} + n_{2,1}\beta^{\rm xHe}_{k,j}\,. \tag{59}$$

The recombination destruction rate of $n_{k,j}$ to adjacent stage $n_{k,j-1}$ and the ionization destruction rate of $n_{k,j}$ to adjacent stage $n_{k,j+1}$, are

$$\begin{aligned} R^{\rm rec}_{k,j} &= n_e\left(\beta^{\rm phr}_{k,j-1} + \beta^{\rm die}_{k,j-1}\right) + n_{1,1}\beta^{\rm xH}_{k,j-1} + n_{2,1}\beta^{\rm xHe}_{k,j-1} \\ R^{\rm ion}_{k,j} &= R^{\rm ph}_{k,j} + n_e\left(\alpha^{\rm cdi}_{k,j} + \alpha^{\rm cea}_{k,j}\right) + n_{1,2}\alpha^{\rm xH^+}_{k,j}\,, \end{aligned} \tag{60}$$

respectively. The summation terms in Eq. 57 account for Auger ionization processes, which skip adjacent ionization stages. All ions of species k from the neutral stage to ionization stage $i \le j-2$ can contribute to the creation rate of $n_{k,j}$ due to their destruction via Auger ionization

$$\left.\frac{dn_{k,j}}{dt}\right|_{\rm aug} = \sum_{i=1}^{j-2} n_{k,i} R^{\rm aug}_{k,i,j}. \tag{61}$$

Similarly, ion k,j can be destroyed by Auger ionization to high ionization final stage m, where $m \ge j+2$,

$$\left.\frac{dn_{k,j}}{dt}\right|_{\rm aug} = -n_{k,j}\sum_{m=j+2}^{k-1} R^{\rm aug}_{k,j,m}\,. \tag{62}$$

In practice, Auger ionization is a viable creation and destruction channel only for $k \ge 4$.

3.8. *Equilibrium Solution*

If there are N_k atomic species included in the cloud model, then there are $N = \sum_k (k+1)$ non-linear rate equations to be solved, one for each $n_{k,j}$. The equilibrium solution is obtained when $dn_{k,j}/dt = 0$ is satisfied for all k and j (see Eqs. 47, 50, 53, 56, and 57). The system of equations is "closed" by enforcing charge density conservation, given by Eq. 9.

The rate equations are non-linear because the collisional ionization and recombination rates for ion k,j include the product of the electron density and the density of ion k,j, and the charge exchange rates include the product of the number densities of the hydrogen and helium ions and the density of ion k,j.

Here, we describe our method of linearizing the systems of equations. We begin be rearranging the rate equations in terms of the ionization fractions,

$$\frac{1}{f_{k,j}}\frac{d f_{k,j}}{dt} = \frac{1}{n_{k,j}}\frac{dn_{k,j}}{dt} = 0\,. \tag{63}$$

As we show below, this formalism allows us to solve for the ratios of the number densities of adjacent ionization stages $n_{k,j+1}/n_{k,j}$. Defining $\Phi_{k,j} \equiv \Phi_{k,j}(n_e, T, J_E) = n_{k,j+1}/n_{k,j}$, the ionization fractions, $f_{k,j}$, are then computed using a recursive formula. Writing $f_{k,j} = P_{k,j}/S_k$, we have

$$P_{k,j} = P_{k,j-1}\Phi_{k,j-1}\,, \qquad S_k = \sum_{j=1}^{k+1} P_{k,j}\,, \tag{64}$$

where by definition $P_{k,1} = 1$. Note that, alternatively, $f_{k,1} = 1/S_k$ and $f_{k,j} = \Phi_{k,j-1} f_{k,j-1}$. Thus, once all $\Phi_{k,j}$ are determined, all ionization fractions are determined from which all ionic number densities can be computed.

In order to linearize the equations, we adopt a method that reduces the problem to solving for a single quantity, the electron density. This requires that we decouple the hydrogen and helium from the metals in order to remove the non-linearity arising from charge exchange with metals. To accomplish this, we first obtain an initial estimate for the hydrogen, helium, and electron densities. Using Brent's method, we employ charge density conservation (Eq. 9) to solve for the equilibrium electron density for a gas cloud composed of hydrogen and helium only. For hydrogen, we apply Eq. 63 and rearrange Eq. 47 to obtain,

$$\Phi_{1,1} = \frac{R^{\rm ph}_{1,1} + n_e\alpha^{\rm cdi}_{1,1}}{n_e\beta^{\rm phr}_{1,1}}\,, \quad f_{1,1} = \frac{1}{1+\Phi_{1,1}}\,, \quad f_{2,1} = \Phi_{1,1} f_{1,1}\,, \tag{65}$$

and for helium we rearrange Eqs. 50 and 56, to obtain

$$\begin{aligned} \Phi_{2,1} &= \frac{R^{\rm ph}_{2,1} + n_e\alpha^{\rm cdi}_{2,1}}{n_e\beta^{\rm phr}_{2,1}}\,, \qquad \Phi_{2,2} = \frac{R^{\rm ph}_{2,2} + n_e\alpha^{\rm cdi}_{2,2}}{n_e\beta^{\rm phr}_{2,2}}\,, \\ f_{2,1} &= \frac{1}{1+\Phi_{2,1}+\Phi_{2,1}\Phi_{2,2}}\,, \quad f_{2,2} = \Phi_{2,1} f_{2,1}\,, \; f_{2,3} = \Phi_{2,2} f_{2,2}\,. \end{aligned} \tag{66}$$

With an initial estimate of the hydrogen, helium, and electron densities, Eq. 57 for the metal ions can now be rearranged for each k,j to obtain the recursion formula

$$\Phi_{k,j} = \frac{R^{\rm ion}_{k,j} + R^{\rm rec}_{k,j} + R^{\rm A\text{-}out}_{k,j} - \Phi^{-1}_{k,j-1} R^{\rm ion}_{k,j-1} - R^{\rm A\text{-}in}_{k,j}}{R^{\rm rec}_{k,j+1}}\,, \tag{67}$$

where $R^{\rm ion}_{k,j}$ and $R^{\rm rec}_{k,j}$ are given by Eq. 60, $R^{\rm ion}_{k,j-1}$ and $R^{\rm rec}_{k,j+1}$ by Eqs. 58 and 59, respectively, and the Auger destruction and creation rates are

$$R^{\rm A\text{-}out}_{k,j} = \sum_{m=j+2}^{k-1} R^{\rm aug}_{kjm}\,, \qquad R^{\rm A\text{-}in}_{k,j} = \sum_{i=1}^{j-2}\left[\prod_{n=i}^{j-1}\Phi^{-1}_{kn}\right] R^{\rm aug}_{kij}\,, \tag{68}$$

obtained from Eqs. 61 and 62. For example, for j = 1–4, we have

$$\begin{aligned} \Phi_{k,1} &= R'_{k,1}/R^{\rm rec}_{k,2}\,, \\ \Phi_{k,2} &= \left(R'_{k,2} - \Phi^{-1}_{k,1}R^{\rm ion}_{k,1}\right)/R^{\rm rec}_{k,3}\,, \\ \Phi_{k,3} &= \left(R'_{k,3} - \Phi^{-1}_{k,2}R^{\rm ion}_{k,2} - \Phi^{-1}_{k,1}\Phi^{-1}_{k,2}R^{\rm aug}_{k,1,3}\right)/R^{\rm rec}_{k,4}\,, \\ \Phi_{k,4} &= \left(R'_{k,4} - \Phi^{-1}_{k,3}R^{\rm ion}_{k,3} - \Phi^{-1}_{k,1}\Phi^{-1}_{k,2}\Phi^{-1}_{k,3}R^{\rm aug}_{k,1,4} - \Phi^{-1}_{k,2}\Phi^{-1}_{k,3}R^{\rm aug}_{k,2,4}\right)/R^{\rm rec}_{k,5}\,. \end{aligned} \tag{69}$$

where we combined the destruction rates into the single term $R'_{k,j} = R^{\rm ion}_{k,j} + R^{\rm rec}_{k,j} + R^{\rm A\text{-}out}_{k,j}$. From the $\Phi_{k,j}$, we apply Eq. 64 to compute the ionization fractions for all metal ions. We then refine the hydrogen and helium ionization fractions by includ-

ing charge exchange with metals ions,

$$\Phi_{1,1} = \frac{R^{\rm ph}_{1,1} + n_{\rm e}\alpha^{\rm cdi}_{1,1} + n_{\rm A}\sum_{\rm k=2}\eta_{\rm k}\sum_{\rm j=2}^{\rm k+1} f_{\rm k,j}\beta^{\rm xH}_{\rm k,j-1}}{n_{\rm e}\beta^{\rm phr}_{1,1} + n_{\rm A}\sum_{\rm k=2}\eta_{\rm k}\sum_{\rm j=1}^{\rm k} f_{\rm k,j}\alpha^{\rm xH^+}_{\rm k,j}},$$

$$\Phi_{2,1} = \frac{R^{\rm ph}_{2,1} + n_{\rm e}\alpha^{\rm cdi}_{2,1} + n_{\rm A}\eta_1 f_{1,2}\beta^{\rm xHe}_{1,1} + n_{\rm A}\sum_{\rm k=3}\eta_{\rm k}\sum_{\rm j=2}^{\rm k+1} f_{\rm k,j}\beta^{\rm xHe}_{\rm k,j-1}}{n_{\rm e}\beta^{\rm phr}_{2,1}}, \quad (70)$$

$$\Phi_{2,2} = \frac{R^{\rm ph}_{2,2} + n_{\rm e}\alpha^{\rm cdi}_{2,2} + n_{\rm A}\eta_1 f_{1,2}\alpha^{\rm xH^+}_{2,2}}{n_{\rm e}\beta^{\rm phr}_{2,2} + n_{\rm A}\eta_1 f_{1,1}\beta^{\rm xH}_{2,2}},$$

We remind the reader that we do not treat charge exchange ionization of metals from ionized helium (which would appear as a additional recombination term in the denominator of the expression for $\Phi_{2,1}$).

Using Brent's method, we iteratively apply Eqs. 67–70 to converge on the full equilibrium solution by enforcing charge density conservation via Eq. 9. The method solves for the logarithm of the equilibrium electron density to a precision of 1×10^{-20}. The high precision is required in order to constrain ions that yield small donations to the free electron pool; mostly these are the elements with the lowest abundances. Since the initial estimate of the hydrogen, helium, and electron density from a zero metallicity gas typically provides $\log n_{\rm e}$ to 2-3 decimal points of accuracy, usually only 5-7 iterations are required to converge $\log n_{\rm e}$ to 20 decimal points of accuracy.

In the case of low ionization clouds, the ions with the least constrained number densities are the high ionization stages of the low abundance species, since they contribute negligibly to the free electron pool. In the case of high ionization clouds, the same applies to the low ionization stages of the low abundance species. In other words, the method's strength is that it best constrains the number densities of the ionic stages that contribute the most to the electron pool. Once all ionization fractions are solved, the ion number densities are computed from $n_{\rm k,j} = f_{\rm k,j} n_{\rm k} = f_{\rm k,j}\eta_{\rm k} n_{\rm A}$.

4. THE OPTICALLY THIN CONSTRAINT

Because we do not yet treat radiative transfer[4] through the cloud models (grid cells), currently HARTRATE is appropriate only for optically thin gas (also see Verner & Iakovlev 1990). By optically thin, we employ the definition that the optical depth is less than unity at the hydrogen ionization edge (13.6 eV), and at both the neutral and singly ionized helium ionization edges (24.6 and 54.4 eV, respectively), which dominate modification of the ionizing SED.

To illustrate how the ionization edges modify the ionizing SED as cloud models become progressively more optically thick, we plot the mean intensity of the attenuated SED transmitted though various Cloudy 13.03 models as a function of photon energy in Figure 5. The black curves are the incident Haardt & Madau (2011) UVB for $z = 0$. The clouds models have metallicity of 0.1 solar. Blue, green and, red curves show the attenuated transmitted spectrum after having passed through cloud models with fixed $\log N({\rm H\,I}) \equiv \log N_{\rm H^0} = 17.5$, 18.0, and 18.5, respectively. Three hydrogen densities are illustrated, $\log n_{\rm H} = -1$, -2, and -3. The ground-state ionization edges of H^0, He^0, and He^+ are shown as vertical dotted lines. For reference, vertical ticks indicate the ground-state ionization edges of Mg^+ (Mg II), C^{+3} (C IV), and O^{+5} (O VI). Clearly, the number density of ionizing photons for these important metal species can be substantially reduced with depth into the cloud model, resulting in ionization structure in the cloud model and lower ionization conditions in the shielded regions.

Since the optical depth is the product of the cross section for bound-free absorption and the column density of the absorbing ion, we can determine the upper limit on the H^0, He^0, and He^+ column densities that satisfy our criterion of an upper limit of unity optical depth at the respective ionization edges. For ground state hydrogen and singly ionized helium, the optical depth at the ionization edge is (Menzel & Pekeris 1935),

$$\tau = N\sigma = 6.304 \times 10^{-18} \cdot \frac{N}{Z^2}\left(\frac{\mu}{m_e}\right)^{-1}, \quad (71)$$

where N is the column density, σ is the bound-free cross section for at the ionization energy from the ground state, Z is the number or protons in the nucleus, and μ is the reduced mass of the electron, $\mu = m_e/(1 + m_e/M_{\rm k})$, where $M_{\rm k}$ is the nuclear mass of species k. For hydrogen, $Z = 1$ and $\mu/m_e = 0.99946$, and for helium, $Z = 2$ and $\mu/m_e = 0.99986$. Thus, for $\tau \leq 1$, the cloud model is constrained to have $N_{\rm H^0} \leq 1.58 \times 10^{17}$ cm^{-2} for neutral hydrogen and $N_{\rm He^+} \leq 6.34 \times 10^{17}$ cm^{-2} for singly ionized helium.

For ground state neutral helium, the optical depth of the ionization edge is (Vardya 1964),

$$\tau = N\sigma = 1.339 \times 10^{-18} \cdot N Z^4_{\rm eff}\left(\frac{\mu}{m_e}\right)^2 \lambda^3 g_{\rm II}, \quad (72)$$

where $Z_{\rm eff} = 1.3343$ is the effective nuclear charge due to screening, $\lambda = 504.19$ Å is the wavelength at the ionization edge, and $g_{\rm II} \simeq 0.827$ is the bound-free Gaunt factor (Menzel & Pekeris 1935). Evaluating, we obtain the constraint $N_{\rm He^0} \leq 2.77 \times 10^{17}$ cm^{-2} for $\tau \leq 1$.

In terms of the limiting column densities, the optically thin constraints place upper limits on the model cloud depth, $L_{\rm max}$, which is to say, in our application, that it places an upper limit on the grid cell size before self-shielding must be treated. Geometrically, $L_{\rm H^0} = N_{\rm H^0}/(f_{\rm H^0} n_{\rm H})$, where $f_{\rm H^0} = n_{\rm H^0}/n_{\rm H}$ is the ionization fraction of neutral hydrogen. When $N_{\rm H^0} = 1.58 \times 10^{17}$ cm^{-2}, then $L_{\rm H^0}$ corresponds to the cloud depth at which the optical depth at the hydrogen ionization edge is unity. Similarly, for neutral helium, the upper limit is $L_{\rm He^0} = N_{\rm He^0}/(f_{\rm He^0} n_{\rm H} \cdot \eta_{\rm He}/\eta_{\rm H})$ for $N_{\rm He^0} = 2.77 \times 10^{17}$ cm^{-2} , where $\eta_{\rm H}$ and $\eta_{\rm He}$ are the abundance fractions of hydrogen and helium, respectively (see Section 3.2). For singly ionized helium, $L_{\rm He^+} = N_{\rm He^+}/(f_{\rm He^+} n_{\rm H} \cdot \eta_{\rm He}/\eta_{\rm H})$ for $N_{\rm He^+} = 6.34 \times 10^{17}$ cm^{-2}.

Assuming a fairly constant ratio $\eta_{\rm He}/\eta_{\rm H} \simeq 0.1$, we can rewrite the cell upper limits as follows,

$$\begin{aligned} L^{\rm max}_{\rm H^0} &\simeq 0.5 \cdot (0.01/f_{\rm H^0})(0.01/n_{\rm H}) \\ L^{\rm max}_{\rm He^0} &\simeq 9 \cdot (0.01/f_{\rm He^0})(0.01/n_{\rm H}) \quad {\rm kpc} \\ L^{\rm max}_{\rm He^+} &\simeq 20 \cdot (0.01/f_{\rm He^+})(0.01/n_{\rm H}). \end{aligned} \quad (73)$$

For the criterion of optically thin radiative transfer, the upper limit on the cloud depth, $L_{\rm max}$, is the minimum of $L_{\rm H^0}$, $L_{\rm He^0}$, and $L_{\rm He^+}$. As the radiation propagates deeper into the cloud, the mean intensity of the SED will be modified by ionization (the SED is "softened" by the removal of high energy photons). As

[4] We are currently implementing and testing self shielding in the code, which we will present in a second paper in this series.

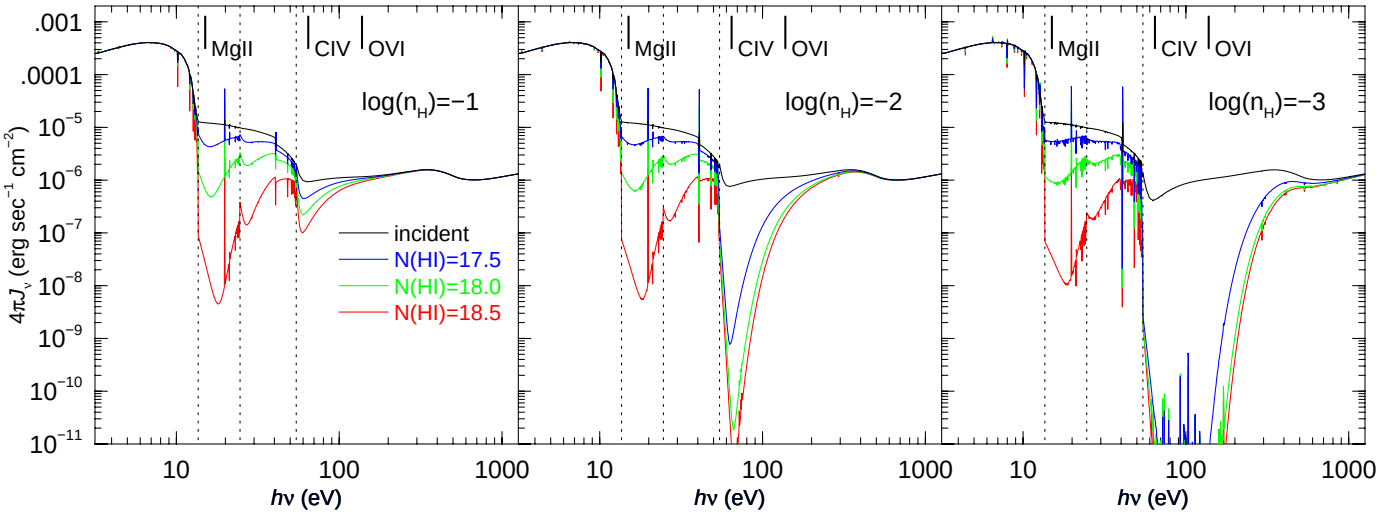

Figure 5. The mean intensity of the attenuated ionizing spectrum transmitted though various cloud models as a function of photon energy [eV]. The black curves are the incident UVB. Blue, green and, red curves are the attenuated spectrum after having passed through cloud models with fixed $\log N_{\rm H^0} = 17.5$, 18.0, and 18.5, respectively. Vertical dotted lines give the ground-state ionization edges of H^0 (H I, 13.6 eV) , He^0 (He I, 24.6 eV), and He^+ (He II, 54.4 eV). For reference, the ground-state ionization edges of Mg^+ (Mg II), C^{+3} (C IV), and O^{+5} (O VI) are shown as vertical ticks. (left) Results for cloud hydrogen number density $\log n_{\rm H} = -1$. (center) Results for $\log n_{\rm H} = -2$. (right) Results for $\log n_{\rm H} = -3$. As $N({\rm H\,I}) \equiv N_{\rm H^0}$ of a cloud model with fixed $n_{\rm H}$ increases, the physical depth of the cloud increases and the softer the ionizing spectrum becomes as more photons are absorbed due to the ionization of hydrogen and helium. This alters the ionization balance of metals such as Mg^+, C^{+3}, and O^{+5} as a function of depth into the cloud. For fixed N(H I), model clouds with lower $n_{\rm H}$ have greater physical depth than higher $n_{\rm H}$ model clouds, resulting in much greater attenuation due to He^+ ionization relative to the hydrogen ionization edge.

such, $L_{\rm max}$ is the depth into the cloud to which the ionization structure is constant.

The minimum comoving cell size for the hydroART simulations is roughly 30 h^{-1} pc (0.03 h^{-1} kpc) and the proper size decreases with redshift in proportion to $1/(1+z)$. From Eq. 73, we see that only in cases where the product of the ionization fraction and the hydrogen number density exceed 10^{-4} does the maximum cell size decrease from the fiducial values of 0.5, 9 and 20 kpc for the respective ionization edges. In Figure 6, we plot the ionization fractions for H^0 (top), He^0 (center), and He^+ (bottom) as a function of hydrogen number density, $\log n_{\rm H}$, for constant density and isothermal optically thin clouds. Four temperatures are presented, $\log T$ = 3, 4, 5, and 6 as black, blue, red, and green curves, respectively. Examining the behavior of the ionization fractions and propagating them through Eq. 73, we find that HARTRATE is currently not valid for "cold" cells ($\log T < 4$) with densities $\log n_{\rm H} > -2$ nor for "warm/hot" cells ($\log T \simeq 5$) with densities $\log n_{\rm H} > -1$.

5. COMPARISON TO CLOUDY

The most important quantities for comparing ionization codes are the ionization fractions. In particular, those of hydrogen and helium are critical since they dictate the conditions of the onset of self shielding to the ionizing radiation. To compare these ionization fractions between HARTRATE and Cloudy 13.03, we ran both codes and created a grid of cloud models while enforcing the optically thin constraint. We present the ionization fractions in Figure 6. The dashed curves are Cloudy models and the solid curves are HARTRATE models. For both codes, we assume constant density isothermal cloud models with no dust, no cosmic ray heating, a metallicity of 10% solar, and a Haardt & Madau (2011) UVB at $z = 0$.

HARTRATE is in general excellent agreement with Cloudy. However, there are deviations of up to a factor of two in $f_{\rm He^0}$ for $\log T \geq 5$ at all $n_{\rm H}$ and for $f_{\rm He^+}$ for $\log T \simeq 3$ at $\log n_{\rm H} > 0$. At these temperature, collisional ionization is becoming more important relative to photoionization. We have not identified the source of the discrepancy with the He^0 ion in this regime. One main difference between HARTRATE and Cloudy is that Cloudy handles recombination levels, whereas HARTRATE assumes two-level ions (ground state and the continuum). In Cloudy, the He^0 ion includes the full helium isoelectronic sequence (Porter et al. 2005).

We now compare the ionization fractions between HARTRATE and Cloudy for the metal ions Mg^+, C^{+3}, and O^{+5}. For this discussion, we slightly modify our notation from Section 3 such that species k in ionization stage j is denoted by the somewhat more familiar notation X^j denoting species X in ionization stage j.

For a constant density gas cloud, the column density of species X in ionization stage j, denoted $N_{\rm X^j}$, is

$$N_{\rm X^j} = n_{\rm X^j} L = f_{\rm X^j} n_{\rm X} L, \tag{74}$$

where the number density of ion X^j is $n_{\rm X^j}$, the ionization fraction (from the ionization model) is $f_{\rm X^j}$, and the number density of species X is $n_{\rm X} = \left(\eta_{\rm X}/\eta_{\rm H}\right) n_{\rm H}$. The quantity L is the cloud depth. Observers often combine the measured H I column density, $N_{\rm HI}$, with ionization modeling to estimate the pathlength through the absorbing gas, using the expression $L = N_{\rm HI}/(f_{\rm H^0} n_{\rm H})$. For our comparison with Cloudy, we adopt this convention because, observationally, $N_{\rm HI}$ is a directly measurable quantity, whereas L is not and must be inferred from the ionization modeling.

Substituting the above expression L into Eq. 74, we obtain the "observer's"expression for the cloud column density for metal ion X^j,

$$\log N_{\rm X^j} = \log N_{\rm HI} + \log\left\{\frac{f_{\rm X^j}}{f_{\rm H^0}}\right\} + \log\left\{\frac{n_{\rm X}}{n_{\rm H}}\right\}, \tag{75}$$

where $n_{\rm X}/n_{\rm H} = \left(\eta_{\rm X}/\eta_{\rm H}\right)$ corresponds to the abundance ratio

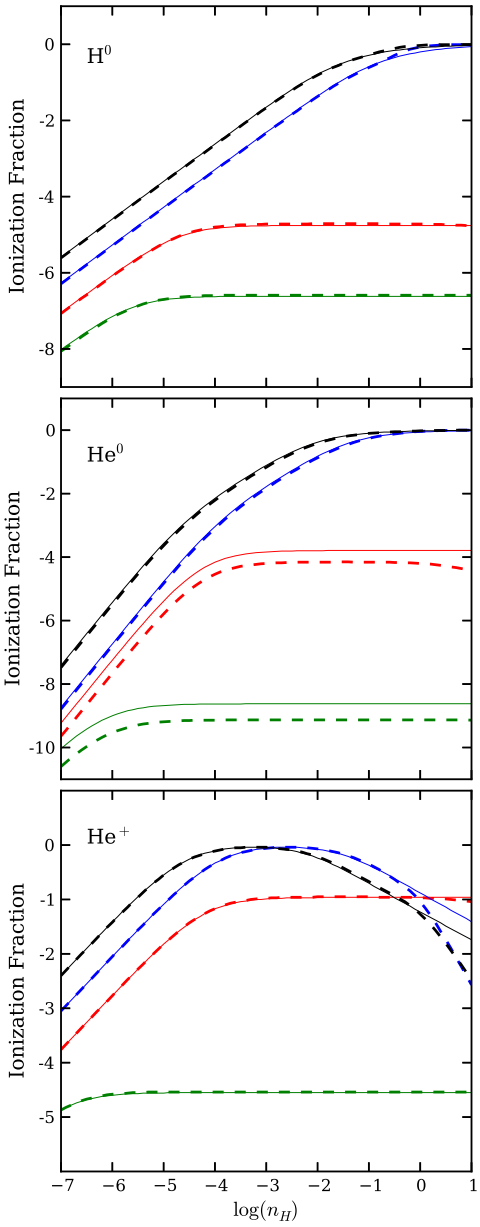

Figure 6. The logarithm of the ionization fractions for H^0 (top), He^0 (center), and He^+ (bottom) as a function of hydrogen number density, $\log n_H$ for optically thin cloud models. Dashed curves are the results from Cloudy and solid curves are the results from HARTRATE. Four temperatures are shown, $\log T = 3$ (black), $\log T = 4$ (blue), $\log T = 5$ (red), $\log T = 6$ (green). Our code HARTRATE is in excellent agreement with Cloudy over a large range of n_H and T, with no more than a factor of 2–3 discrepancies for He^0 at $\log T \geq 5$ and a divergence for He^+ at $\log T \leq 4$ for $\log n_H > 0$.

(X/H).

The second term on the right hand side of Equation 75 is known as the ionization correction, $IC = \log\{f_{Xj}/f_{H^0}\}$. This term is the critical quantity from ionization models that, for observational work, allows the *measured* column densities to be used as constraints for inferring gas phase abundances by solving $\log(X/H) = \log N_{Xj} - \log N_{HI} - IC$. However, our application with the simulations will be slightly different (see Churchill et al. 2014); we know the line-of-sight pathlength through the cell and the elemental abundances in the grid cell in the simulation and employ HARTRATE to determine the cell column densities using Eq. 74.

Given the methods of application described above, we focus on the ionization correction as the central quantity for comparing HARTRATE and Cloudy. We define

$$\Delta IC = \log\left\{\frac{f_{Xj}}{f_{H^0}}\right\} - \log\left\{\frac{f_{Xj}}{f_{H^0}}\right\}_{Cloudy}, \quad (76)$$

which, for fixed N_{HI} and n_X/n_H, provides a direct measure of logarithmic difference in the calculated column density between the two ionization models,

$$(\log N_{Xj})_{HARTRATE} - (\log N_{Xj})_{Cloudy} = \Delta IC. \quad (77)$$

We computed ΔIC as a function of n_H and T over the range $-7 \leq \log n_H \leq 0$ and $2 \leq \log T \leq 7$ for constant density isothermal cloud models. We apply Eq. 73 to ensure that the clouds are optically thin at the hydrogen and helium ionization edges (which means N_{HI} varies with n_H). For both HARTRATE and Cloudy, we assume no dust, no cosmic ray heating, a metallicity of 10% solar, and a Haardt & Madau (2001, 2011) UVB at $z = 0$ for the ionizing spectrum.

In Figure 7, we plot smoothed ΔIC surfaces as a function of $\log n_H$ and $\log T$ for the three commonly observed ions, Mg^+ (left panel), C^{+3} (center), and O^{+5} (right). The presented ranges of the density and temperature vary slightly from ion to ion based on the appropriate ranges of gas phase in which they are dominant (see Churchill et al. 2014). The values of ΔIC are provided in the color bar.

Since typical uncertainties in observed column density measurements are $\delta \log N \simeq \pm 0.05$ in the logarithm, values of $\Delta IC \leq \pm 0.05$ between the two ionization models would be consistent with typical measurement errors in $\log N_{Xj}$. This level of uncertainty corresponds to the green area of the surface in Figure 7. Thus, the green area provides the $\log n_H$–T ranges over which the difference in the ionization correction between HARTRATE and Cloudy are within reasonable observational measurement uncertainties, and can therefore be considered to yield column densities that are consistent within practical errors.

The larger departures in ΔIC (blue and red regions) are due to (1) the linearization method employed for HARTRATE (see Section 3.8), and (2) the convention within Cloudy to fix $\log f_{Xj} = -30$ or -50 in the cases of very small ionization fractions. For (1), it is because we converge the rate matrix using charge density conservation, per Eq. 9, so that ions contributing negligibly to the free electron density do not have robustly constrained ionization fractions. Since, in these cases, the ionization fractions are typically on the order of 10^{-20} or lower (recall that we conserve charge to this tolerance level), these regions of gas phase space are not abundant in the ion. As such, these phase space regions do not contribute to absorption lines from the ion, and since one of our main goals is to study the absorption properties of the gas in the simulations (e.g., Churchill et al. 2014), the absolute accuracy in the ionization correction for these ions does not impact our science goals.

6. CONCLUSIONS

We have presented the code HARTRATE for computing the equilibrium ionization conditions for astrophysical gaseous environments. The main motivation for developing HARTRATE is to apply it to AMR cosmological simulation in order to study the chemical and ionization conditions of the

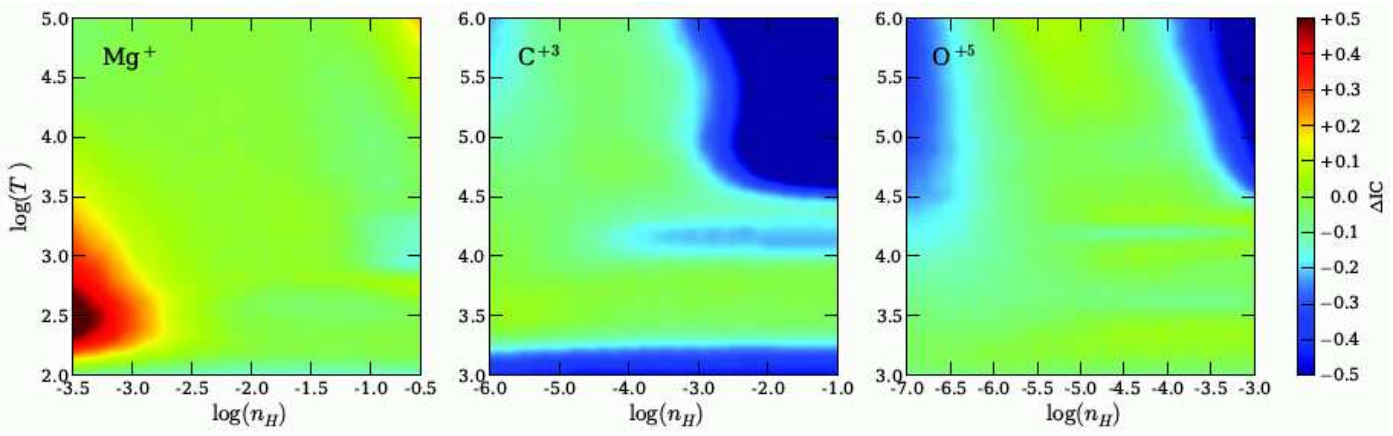

Figure 7. A comparison of the ionization corrections, IC = $\log\{f_{X^j}/f_{H^0}\}$ between HARTRATE and Cloudy. The logarithmic difference if the ionization corrections, ΔIC, is plotted as a function of hydrogen number density and temperature of the cloud model. ΔIC = 0 indicates full agreement between the models. (left) ΔIC for $X^j = Mg^+$. (center) ΔIC for C^{+3}. (right) ΔIC for O^{+5}. The green shading represents ΔIC $\simeq \pm 0.05$, where agreement between the two codes is within the typical observational uncertainties of measured column densities. Blue and red areas are regions where the ionization fractions of the metal ions are vanishingly small and are, for the most part, an artifact of the manner in which such ionization fractions are output by Cloudy (see text).

circumgalactic medium in simulated galaxies using the absorption line technique. For a first application of the code to AMR cosmological simulations, see Churchill et al. (2014). A stand-alone version of HARTRATE also exists, and has been applied to observational data (see Churchill et al. 2012; Kacprzak et al. 2012).

The physical gas processes included in HARTRATE are photoionization, Auger ionization, direct collisional ionization, excitation auto-ionization, charge exchange ionization, radiative recombination, dielectronic recombination, and charge exchange recombination. Currently, the code handles only optically thin gas. Treatment of optically thick gas will be presented in a companion paper.

HARTRATE is designed to take a minimum number of inputs to define a "cloud" model. The inputs are the gas hydrogen density, $n_{\rm H}$, equilibrium temperature, T, and the mass fractions of all atomic species. To define the ionizing spectrum, the required inputs are the redshift, z, for the Haardt & Madau (2011) UVB, and if desired, the masses, ages, metallicities, and locations of stellar populations for the Starburst99 (Leitherer et al. 1999) SED models.

We compared HARTRATE to Cloudy 13.03 by examining the ionization fractions of neutral hydrogen, neutral helium, and singly ionized helium. In the optically thin regime, the ionization fractions are highly consistent, except for a factor of 2–3 difference in the neutral helium values for $\log T \geq 5$. We also presented a comparison of the ionization corrections for the three metal ions Mg^+, C^{+3}, and O^{+5} that are responsible for the Mg II $\lambda\lambda 2796, 2803$, C IV $\lambda\lambda 1548, 1550$, and O VI $\lambda\lambda 1031, 1037$ doublets commonly studied in absorption. Over the $\log n_{\rm H}$–T phase space $-7 \leq \log n_{\rm H} \leq 0$ and $3 \leq \log T \leq 6$, the logarithmic difference in the ionization corrections agreed with in ± 0.05. This agreement is within typical uncertainties of measured logarithmic column densities.

Future improvements to the code include (1) self shielding so that optically thick cloud models can be treated, and (2) radiative transfer through the simulation box to handle frequency dependent shadowing from structures intervening to luminous sources. These will be reported in future papers.

The stand-alone version of HARTRATE, is available on-line at *http://astronomy.nmsu.edu/cwc/Software/Ioncode/*. This code is useful for generating grids of optically thin model clouds as a function of hydrogen density, temperature, and redshift. The output includes the equilibrium ionization fractions, number densities, photoionization rates, and ionization and recombination rate coefficients for all collisional processes for all ions. Once self-shielding is added, the code will be updated on-line and will be capable of generating optically thick cloud models.

CWC, EK, and JRV were partially supported through grants HST-AR-12646 and HST-GO-13398 provided by NASA via the Space Telescope Science Institute, which is operated by the Association of Universities for Research in Astronomy, Inc., under NASA contract NAS 5-26555. CWC acknowledges assistance through the NASA New Mexico Space Grant Consortium (NMSGC) Research Enhancement Program, which supported AM. JRV acknowledges support through an NMSGC Graduate Research Fellowship. Thanks to R. Sutherland for helpful email exchanges and to G. Ferland for insightful conversations during his visit to NMSU. Much gratitude goes to D. Verner for providing publicly available electronic tables for photoionization, recombination, collisional ionization, and autoionization and some supporting computational subroutines (*http://www.pa.uky.edu/∼verner/*). We are grateful for the work of N. Badnell, R. Bingham, G. Duxbury, and H. Summers of the Atomic and Molecular Diagnostic Processes in Plasmas group (*http://amdpp.phys.strath.ac.uk/tamoc/*), who provided radiative and dielectronic recombination rates. We also thank P. Stancil, D. Schultz, J. Wang, M. Raković, J. Kingdon, and A. Dalgarno, of the Oakridge National Lab UGA Charge Transfer Database for Astrophysics (*http://www-cfadc.phy.ornl.gov/astro/ps/data/*).

REFERENCES

Abel, T., & Wandelt, B. D. 2002, MNRAS, 330, L53
Agertz, O., Moore, B., Stadel, J., et al. 2007, MNRAS, 380, 963
Agertz, O., & Kravtsov, A. V. 2014, arXiv:1404.2613
Aldrovandi, S. M. V., & Pequignot, D. 1973, A&A, 25, 137
Altun, Z., Yumak, A., Yavuz, I., Badnell, N. R., Loch, S. D., & Pindzola, M. S. 2007, A&A, 474, 1051
Arnaud M., & J. Raymond R. 1992, ApJ, 398, 394
Arnaud, M., & Rothenflung, R. 1985, A&AS, 60 425
Asplund, M., Grevesse, N., Sauval, A. J., & Scott, P. 2009, ARA&A, 47, 481
Aubert, D., & Teyssier, R. 2008, MNRAS, 387, 295

Badnell, N. R. 1986, J. Phys. B, 19, 3827
Badnell, N. R. 2003, ApJS, 167, 334
Badnell, N. R., O'Mullane, M. G., Summers, H. P., et al. 2003, A&A, 406, 1151
Behroozi, P. S., Conroy, C., & Wechsler, R. H. 2010, ApJ, 717, 379
Behroozi, P. S., Wechsler, R. H., & Conroy, C. 2013, ApJ, 770, 57
Bergeron, J., & Stasińska, G. 1986, A&A, 169, 1
Bordoloi, R., Tumlinson, J., Werk, J. K., et al. 2014, arXiv:1406.0509
Bothwell, M. S., Maiolino, R., Kennicutt, R., et al. 2013, MNRAS, 433, 1425
Cen, R., & Fang, T. 2006, ApJ, 650, 573
Ceverino, D., Dekel, A., & Bournaud, F. 2010, MNRAS, 404, 2151
Ceverino, D., Dekel, A., Mandelker, N., et al. 2012, MNRAS, 420, 3490
Ceverino, D., & Klypin, A. 2009, ApJ, 695, 292
Ceverino, D., Klypin, A., Klimek, E., et al. 2014, MNRAS, 442, 1545
Chieffi, A., & Limongi, M. 2013, ApJ, 764, 21
Churchill, C. W. 1997, Ph.D. Thesis, University of California, Santa Cruz
Churchill, C. W., & Le Brun, V. 1998, ApJ, 499, 677
Churchill, C. W., Kacprzak, G. G., Steidel, C. C., et al. 2012, ApJ, 760, 68
Churchill, C. W., Mellon, R. R., Charlton, J. C., Jannuzi, B. T., Kirhakos, S., Steidel, C. C., & Schneider, D. P. 2000, ApJS, 130, 91
Churchill, C. W., Rigby, J. R., Charlton, J. C., & Vogt, S. S. 1999, ApJS, 120, 51
Churchill, C. W., Vander Vliet, J. R, Trujillo-Gomez, S., et al. 2014, ApJ, submitted
Churchill, C. W., & Vogt, S. S. 2001, AJ, 122, 679
Davé, R., Oppenheimer, B. D., & Finlator, K. 2011, MNRAS, 415, 11
Davé, R., Oppenheimer, B. D., & Finlator, K. 2011b, MNRAS, 415, 11
Dittmann, O. J., & Koeppen, J. 1995, A&A, 297, 671
Dolag, K., Borgani, S., Schindler, S., Diaferio, A., & Bykov, A. M. 2008, Space Sci. Rev., 134, 229
Dopita, M. A., & Sutherland, R. S. 2003, Astrophysics of the Diffuse Universe, Springer
Draine, B. T. 2011, Physics of the Interstellar and Intergalactic Medium, Princeton University Press, ISBN: 978-0-691-12214-4 (Table 1.4, p8)
Evans, J. L. 2008, Ph.D., New Mexico State University, http://astronomy.nmsu.edu/jlevans/dissertation/
Evans, J. L., Churchill, C. W., Murphy, M. T., Nielsen, N. M., & Klimek, E. S. 2013, ApJ, 768, 3
Faucher-Giguère, C.-A., Lidz, A., Zaldarriaga, M., & Hernquist, L. 2009, ApJ, 703, 1416
Ferland, G. J., Korista, K. T., & Verner D. A. 1997, ApJ, 481, L115
Ferland, G. J., Korista, K. T., Verner, D. A., et al. 1998, PASP, 110, 761
Ferland, G. J., Porter, R. L., van Hoof, P. A. M., et al. 2013, RMxAA, 49, 137
Ferland, G. J., Hazy, A Brief Introduction to Cloudy 96, University of Kentucky Department of Physics and Astronomy Internal Report
Finlator, K., Özel, F., & Davé, R. 2009, MNRAS, 393, 1090
Ford, A. B., Davé, R., Oppenheimer, B. D., et al. 2013a, arXiv:1309.5951
Ford, A. B., Oppenheimer, B. D., Davé, R., et al. 2013b, MNRAS, 432, 89
Fox, A. J., Ledoux, C., Petitjean, P., & Srianand, R. 2007b, A&A, 473, 791
Fox, A. J., Petitjean, P., Ledoux, C., & Srianand, R. 2007a, A&A, 465, 171
Fumagalli, M., Prochaska, J. X., Kasen, D., et al. 2011, MNRAS, 418, 1796
Gnat, O., & Sternberg, A. 2007, ApJS, 168, 213
Gnedin, N. Y., & Abel, T. 2001, New Astronomy, 6, 437
González Delgado, R. M., Cid Fernandes, R., García-Benito, R., et al. 2014, ApJ, 791, L16
Haardt, F., & Madau, P. 2001, in Clusters of Galaxies and the High Redshift Universe Observed in X-rays, XXIst Moriond Astrophysica Meeting, eds. D. M. Neumann & J. T. V. Tran, 64
Haardt, F., & Madau, P. 2011, ApJ, arXiv:1105.2039
Hopkins, P. F., Keres, D., Onorbe, J., et al. 2013a, arXiv:1311.2073
Hopkins, P. F., Narayanan, D., Murray, N., & Quataert, E. 2013b, MNRAS, 433, 69
Howell, L. H., & Greenough, J. A. 2003, Journal of Computational Physics, 184, 53
Hu, W., Chen, C., Fang, D., Wang, Y., Lu, F., & Yang, F. 1996, J. Phys. B: At. Opt. Phys., 29, 2887
Humlíček, J. 1979, Journal of Quantitative and Radiative Transfer, 21, 309
Hummels, C. B., Bryan, G. L., Smith, B. D., & Turk, M. J. 2013, MNRAS, 430, 1548
Iliev, I. T., Ciardi, B., Alvarez, M. A., et al. 2006, MNRAS, 371, 1057
Iliev, I. T., Whalen, D., Mellema, G., et al. 2009, MNRAS, 400, 1283
Iwamoto, K., Brachwitz, F., Nomoto, K., et al. 1999, ApJS, 125, 439
Jenkins, E. B. 1996, ApJ, 471, 292
Kaastra, J. S., & Mewe, R. 1993, A&AS, 97, 443
Kacprzak, G. G., Churchill, C. W., Steidel, C. C., Spitler, L. R., & Holtzman, J. A. 2012, MNRAS, 427, 3029
Kim, C.-G., Ostriker, E. C., & Kim, W.-T. 2013, ApJ, 776, 1
Kingdon, J. B., & Ferland, G. J. 1996, ApJS, 106, 205
Klypin, A., Kravtsov, A. V., Bullock, J. S., & Primack, J. R. 2001, ApJ, 554, 903
Kravtsov, A. V. 1999, Ph.D. Thesis, New Mexico State University
Kravtsov, A. V., Gnedin, O. Y., & Klypin, A. A. 2004, ApJ, 609, 482
Lanzetta, K. M., Bowen, D. V., Tytler, D., & Webb, J. K. 1995, ApJ, 442, 538
Lehner, N., Howk, J. C., Tripp, T. M., et al. 2013, ApJ, 770, 138
Leitherer, C., Schaerer, D., Goldader, J. D., et al. 1999, ApJS, 123, 3
Lilly, S. J., Carollo, C. M., Pipino, A., Renzini, A., & Peng, Y. 2013, ApJ, 772, 119
Mannucci, F., Cresci, G., Maiolino, R., Marconi, A., & Gnerucci, A. 2010, MNRAS, 408, 2115
Mathes, N. L., Churchill, C. W., Kacprzak, G. G., et al. 2014, arXiv:1406.2314
Menzel, D. H., & Pekeris, C. L. 1935, MNRAS, 96, 77
Mihalas, D., & Weibel-Mihalas, B. 1999, Foundations of Radiation Hydrodynamics, Courier Dover Publications
Moster, B. P., Naab, T., & White, S. D. M. 2013, MNRAS, 428, 3121
Munshi, F., Governato, F., Brooks, A. M., et al. 2013, ApJ, 766, 56
Muzahid, S. 2014, ApJ, 784, 5
Nielsen, N. M., Churchill, C. W., & Kacprzak, G. G. 2013b, ApJ, 776, 115
Nielsen, N. M., Churchill, C. W., Kacprzak, G. G., & Murphy, M. T. 2013a, ApJ, 776, 114
Norman, M. L., Reynolds, D. R., & So, G. C. 2009, American Institute of Physics Conference Series, 1171, 260
Nussbaumer, H., & Storey, P. J. 1983, A&A, 126, 75
Nussbaumer, H., & Storey, P. J. 1986, A&AS, 64, 545
Nussbaumer, H., & Storey, P. J. 1987, A&AS, 69, 123
Petkova, M., & Springel, V. 2009, MNRAS, 396, 1383
Porter, R. L., Bauman, R. P., Ferland, G. J., & MacAdam, K. B. 2005, ApJ, 622, L73
Oppenheimer, B. D., & Schaye, J. 2013, MNRAS, 434, 1043
Razoumov, A. O., Norman, M. L., Prochaska, J. X., & Wolfe, A. M. 2006, ApJ, 645, 55
Reynolds, D. R., Hayes, J. C., Paschos, P., & Norman, M. L. 2009, Journal of Computational Physics, 228, 6833
Rosdahl, J., Blaizot, J., Aubert, D., Stranex, T., & Teyssier, R. 2013, MNRAS, 436, 2188
Salpeter, E. E. 1955, ApJ, 121, 161
Sánchez Almeida, J., Elmegreen, B. G., Muñoz-Tuñón, C., & Elmegreen, D. M. 2014, A&A Rev., 22, 71
Savage, B. D., & Sembach, K. R. 1991, ApJ, 379, 245
Schneider, D. P., et al. 1993, ApJS, 87, 45
Schure, K. M., Kosenko, D., Kaastra, J. S., Keppens, R., & Vink, J. 2009, A&A, 508, 751
Seaton, M. J. 1959, MNRAS, 119, 81
Schawinski, K., Urry, C. M., Simmons, B. D., et al. 2014, MNRAS, 440, 889
Sembach, K. R., & Savage, B. D. 1992, ApJS, 83, 147
Shull, J. M., & Van Steenberg, M. 1982, ApJS, 48, 95
Simcoe, R. A., Sargent, W. L. W., Rauch, M., & Becker, G. 2006, ApJ, 637, 648
Stinson, G. S., Dalcanton, J. J., Quinn, T., Kaufmann, T., & Wadsley, J. 2007, ApJ, 667, 170
Stocke, J. T., Keeney, B. A., Danforth, C. W., et al. 2013, ApJ, 763, 148
Stocke, J. T., Penton, S. V., Danforth, C. W., Shull, J. M., Tumlinson, J., & McLin, K. M. 2006, ApJ, 641, 217
Sutherland, R. S., & Dopita, M. A. 1993, ApJS, 88, 253
Tremonti, C. A., Heckman, T. M., Kauffmann, G., et al. 2004, ApJ, 613, 898
Trujillo-Gomez, S., Klypin, A., Colin, P., et al. 2013, arXiv:1311.2910
Tumlinson, J., Thom, C., Werk, J. K., et al. 2011, Science, 334, 948
Tumlinson, J., Thom, C., Werk, J. K., et al. 2013, ApJ, 777, 59
Vander Vliet, J. R., Churchill, C.W., Trujillo-Gomez, S., et al. 2014a, ApJ, in preparation
Vander Vliet, J. R., Churchill, C.W., Trujillo-Gomez, S., et al. 2014b, ApJ, in preparation
Vardya, M. S. 1964, ApJS, 8, 277
Vasiliev, E. O. 2011, MNRAS, 414, 3145
Vasiliev, E. O., Ryabova, M. V., & Shchekinov, Y. A. 2013b, arXiv:1312.4364
Verner, D. A., & Iakovlev, D. G. 1990, Ap&SS, 165, 27
Verner, D. A., & Iakovlev, D. G. 1995, A&AS, 109, 125
Verner, D. A., Ferland, G. J., Korista, K. T., & Iakovlev, D. G. 1996, ApJ, 465, 487
Voronov, G. S. 1997, Atomic Data and Nuclear Data Tables, 65, 1
Werk, J. K., Prochaska, J. X., Tumlinson, J., et al. 2014, arXiv:1403.0947
Whalen, D., & Norman, M. L. 2006, ApJS, 162, 281
Wiersma, R. P. C., Schaye, J., & Smith, B. D. 2009, MNRAS, 393, 99
Wise, J. H., & Abel, T. 2011, MNRAS, 414, 3458